学位論文

Electronic and magnetic structures of iron-nitride atomic layers on Cu(001)

(Cu(001)基板上鉄窒化物原子層膜の
電子・磁気構造の研究)

平成 28 年 12 月博士（理学）申請

東京大学大学院理学系研究科
物理学専攻

髙橋　文雄

Abstract

Iron nitride in iron-rich phases is known to possess rich ferromagnetism such as large saturation magnetization and high magnetic anisotropy, and thus expected to replace existing neodymium magnet as a rare-earth free alternate. The growth in a single phase has been a long-standing problem for iron nitride, which hinders a full characterization of intrinsic physical properties. Recently, the successful epitaxial growth of single-phase γ'-Fe_4N has been reported, and macroscopic properties of the system can be understood in terms of the strong hybridization between Fe and N states. Meanwhile, site-selective electronic and magnetic states as well as its interplay with structure/dimensionality of γ'-Fe_4N has remained elusive for lack of a detailed study in an atomic-layer limit.

In the present work, we establish a growth method and characterize the electronic/magnetic structures of γ'-Fe_4N atomic layers on Cu(001). First, we conduct detailed scanning tunneling microscopy (STM) measurements on the monolayer γ'-Fe_4N/Cu(001), to elucidate the nature of an Fe_2N plane in γ'-Fe_4N. The observed topographic images drastically change depending on a tip-surface distance unlike in pure transition-metal systems. This is attributed to a spatial variation in local density of states in a vacuum side, leading to the shift in an orbital character of the states dominantly detected by the tip with respect to the distance. More generally, this observation could be the first experimental demonstration of the orbital-selective tunneling process inherent in any STM measurements.

A large overlap between the Fe and N states possibly leads to the itinerant electronic states of the monolayer γ'-Fe_4N. This in fact renders the ferromagnetism of the sample sensitive to an atomic structure, namely, degree of surface lattice ordering as discussed in the next part. It turns out that an atomic point defect modulates the surrounding electronic structures in a large area, resulting in deterioration of the ideal sample ferromagnetism. This emphasizes the significant impact of a structural imperfection in an atomic scale on the entire physical properties of the system, which is previously overlooked in macroscopic observations on ferromagnet.

Finally, we report the growth of ordered multilayer γ'-Fe_4N on Cu(001). The strong two-dimensionality originating from the Fe-N hybridization enables a precise stacking of γ'-Fe_4N even in an atomic-layer limit, which makes it possible to scrutinize the layer-by-layer electronic and magnetic states realized in γ'-Fe_4N. The thickness dependence of the electronic structures and magnetic moments of the system has been investigated in detail, the origin of which is perfectly interpreted with the help of first-principle calculations.

Contents

Chapter 1

Introduction

1.1 Background

1.1.1 Transition metal

Transition metal (TM) exhibits rich physical properties originating from unpaired electrons in d shells [1]. An elemental TM possesses a high crystallinity with either the body-centered cubic (bcc), face-centered cubic (fcc), or hexagonal close-packed (hcp) structure at room temperature (RT) and ambient pressure [2]. Compared with typical metals, TMs in a bulk form show fruitful properties such as high melting point and superconducting transition temperature, and a wide variety of magnetism [3–5]. The ground state of almost all the TMs is paramagnetic at ambient pressure. Meanwhile, Fe, Co, and Ni in the $3d$ group are known to show a spontaneous ferromagnetic ordering in an elemental form, with magnetic moments of a couple μ_{B}/atom (where μ_{B} is Bohr magneton) and Curie temperature far above RT [6]. The robust ferromagnetism of $3d$ TMs, in addition to cheapness and abundance as resources, has attracted much interest in terms of both basic research and application. Furthermore, the nature of d orbitals, represented by moderate localization and relatively small spin-orbit coupling compared to outer orbitals, renders physical properties of d-electron systems sensitive to surroundings, e.g. an atomic coordination, crystal field, or hybridization with the neighboring states [7]. This, in other words, makes it easy to tailor the electronic and magnetic properties by changing composition, combination, or dimension of the materials. In fact, lots of novel findings recently discovered in the field of magnetism are related to the spin-polarized nature of $3d$-TM-based ferromagnets: giant, tunneling, and colossal magnetoresistance effects [8–13], as well as large magnetic anisotropy of neodymium and $L1_0$-ordered magnets [14–17].

1.1.2 3*d* transition metal nitride

3*d* TMs tend to form a strong bonding to light elements with large electronegativity. It has been widely reported that the nitridation of 3*d* TMs not only improves chemical stability of the elements, but possibly adds another function to the system [18]. The theoretical observation anticipates that all the 3*d* TMs except for Cu and Zn can form relatively stable nitride in the composition of TM_4N with either a cubic or tetragonal crystal structure[1]; the magnetism of the ground states ranges from nonmagnetic, ferrimagnetic, to ferromagnetic [19]. In particular, ferromagnetic TM_4N (TM = Mn, Fe, Co) has been under intense research because of the perpendicular magnetic anisotropy (Mn_4N) [20–22], high spin polarization and large saturation magnetization M_s (Fe_4N, Co_4N) [23–26]. Further, these ferromagnetic TM_4N can be epitaxially grown on common substrates of $LaAlO_3$(001), MgO(001), or $SrTiO_3$(001) [22, 23, 27, 28]. Such a good epitaxy with the substrate possibly facilitates a precise control of the system dimension from a bulk, film to atomic-layer limit, in which the peculiar electronic and magnetic states are realized in 3*d*-TM-based ferromagnets [29–36].

1.1.3 Iron nitride γ'-Fe_4N

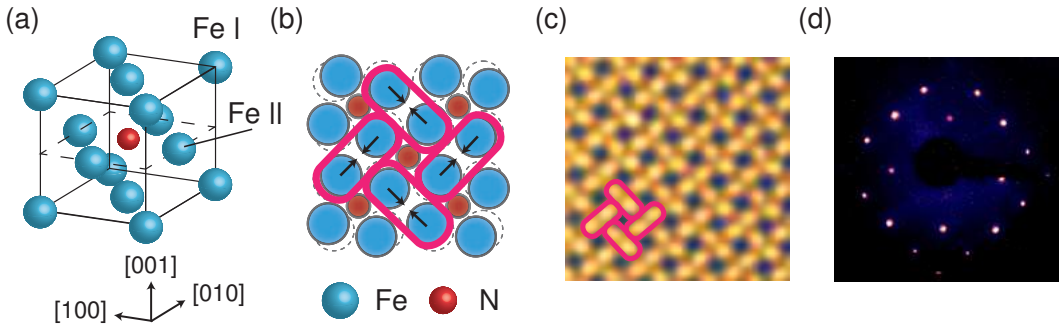

Figure 1.1: Basics of γ'-Fe_4N on Cu(001). (a) Bulk crystal structure of γ'-Fe_4N. A dotted parallelogram represents an Fe_2N plane. (b) Schema of $p4g(2 \times 2)$ surface reconstruction. From an unreconstructed $c(2 \times 2)$ coordination (dotted circles), each two of Fe atoms dimerizes in two perpendicular directions indicated by arrows. For (a) and (b), large (small) spheres represent Fe (N) atoms. (c) Atomically-resolved image (2.5×2.5 nm^2, sample bias $V_s = 0.25$ V, tunneling current $I = 45$ nA) of the surface-reconstructed Fe_2N plane. The dimerization of Fe atoms is indicated by encirclement. (d) LEED pattern with the $p4g(2\times2)$ symmetry, taken with the incident electron energy of 100 eV.

[1]The metastability of TM_4N (TM = Cu, Zn) arises from the fully-occupied 3*d* shell of the TM elements.

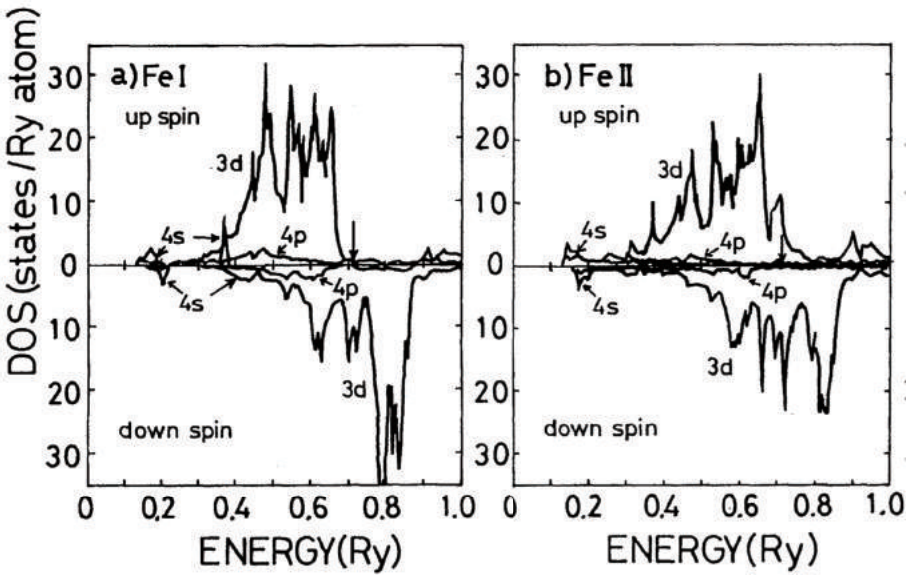

Figure 1.2: Local DOS calculated for (a) FeI and (b) FeII sites of Fe_4N presented in Ref. 41. The Fermi energy is indicated by vertical arrows.

Among all the TM_4N, Fe_4N is theoretically expected to be most energetically stable with a so-called γ'-type crystal structure [19], in which one N atom occupies the center of the fcc Fe lattice as shown in Fig. 1.1(a) . Due to a small lattice mismatch between the bulk crystals of γ'-Fe_4N (3.80 Å) and Cu(001) (3.62 Å) [37, 38], the γ'-Fe_4N can be epitaxially grown on metallic Cu(001). The topmost layer of the γ'-Fe_4N/Cu(001) is known to always consist of the Fe_2N plane in a bulk Fe_4N crystal structure [38–40]. Accordingly, the surface Fe_2N plane takes reconstruction to the $p4g(2\times2)$ coordination, in which the Fe atoms dimerize in two perpendicular directions as illustrated in Fig. 1.1(b). The $p4g(2 \times 2)$ coordination gains total energy in the ferromagnetic ground states, while the nonmagnetic ground states prefers the original $c(2 \times 2)$ coordination [38]. This surface reconstruction can be visualized directly by STM imaging as shown in Fig. 1.1(c), and the corresponding low energy electron diffraction (LEED) pattern of the surface is also observed [Fig. 1.1(d)].

Under the coordination shown in Fig. 1.1(a), two non-equivalent Fe sites FeI and FeII exist, those without and with a bonding to a N atom, respectively. The difference in the site results in the different electronic and magnetic states: FeI and FeII have an electron configuration of $3d^7 4s$ and $3d^8 4s$, as well as the magnetic moment of 3 μ_B and 2 μ_B, respectively [37, 42]. The spin-polarized band calculation in Ref. 41 emphasizes the site dependence of the local density of states (DOS) as shown in Fig. 1.2. At the FeI site, the up-spin band is almost fully-occupied while contains some holes at the Fe FeII site. In contrast to nearly the same occupation into the up-spin band, the number of the down-spin electrons at the FeI and FeII sites are

2.3 and 3.2, respectively. Therefore, the electrons occupied in the down-spin band is responsible for the inequality of the electronic population.

The previous experiments report $M_{\rm s}$ of 2.3 $\mu_{\rm B}$/atom for the bulk γ'-Fe_4N [42], comparable to that of 2.2 $\mu_{\rm B}$/atom for a pristine bulk Fe [37]. The theoretical study points out almost full spin polarization around the Fermi energy $E_{\rm F}$ [43], which has already been applied to magnetic tunneling junctions revealing large inverse tunnel magnetoresistance effect [26]. Thin films of the γ'-Fe_4N show an in-plane easy magnetization [44, 45] in contrast to metastable fcc Fe with a complex spin-spiral structure in the ground state [36, 46]. This difference in the magnetic structure apparently originates from the nitridation of the Fe atoms, which leads to a strong mixing between Fe and N states of the γ'-Fe_4N [19]. This hybridization turns out to be responsible for the unique electronic and magnetic states realized in the γ'-Fe_4N.

1.2 Purpose of the present study

In bulk and thick-film forms, γ'-Fe_4N samples with a high crystallinity can be obtained by molecular beam epitaxy [27] or an Fe deposition under a flux of N from a rf source [38, 39]. A good quality of the samples has made it possible to investigate macroscopic properties of the thick γ'-Fe_4N. On the other hand, for lack of a growth method for ordered γ'-Fe_4N atomic layers, the relationship between structure/dimensionality and the electronic/magnetic states has not been revealed so far in element- and site-selective manners.

In the present study, we succeed in fabricating well-ordered atomic layers of γ'-Fe_4N on a Cu(001) substrate, and conduct a full characterization of the physical properties by utilizing scanning tunneling microscopy/spectroscopy (STM/STS), x-ray absorption spectroscopy/magnetic circular dichroism (XAS/XMCD), and first-principles calculations. A complementary study from both microscopic and macroscopic points of views not only gives novel findings on the electronic and magnetic structures realized in the γ'-Fe_4N atomic layers on Cu(001), but fills the gap between past observations on the present system.

The previous STM works on the γ'-Fe_4N/Cu(001) report different topographic images with the $p4g(2 \times 2)$ [38] and $c(2 \times 2)$ [45] symmetry irrespective of the same surface structures confirmed by the LEED observations. This discrepancy between the images, possibly originating from the difference in the detected electronic structures, can be fully understood by the orbital-selective tunneling process in the STM measurement discussed in Chap. 4. As for the magnetism of the monolayer γ'-Fe_4N/Cu(001), the past XAS/XMCD study reports ferromagnetism with much small magnetic moments compared to the theoretical expectation [45]. The reason for the observed drop in the magnetic moments is clarified by atomically-

resolved STS observations in Chap. 5, which demonstrates the extensive impact of an atomic-scale disorder on the surrounding electronic structures. Finally, in Chap. 6, we present a new growth method to prepare the γ'-Fe_4N atomic layers on Cu(001), and discuss the origin of the thickness-dependent electronic and magnetic properties of the system.

Chapter 2

Experimental methods

2.1 X-ray absorption spectroscopy

X-ray absorption spectroscopy (XAS) is a conventional technique utilizing the photon absorption and subsequent excitation of core electrons into unoccupied states. Combined with an energy-tunable light produced from synchrotron radiation source, this technique can extract detailed information on the sample electronic structures at specific absorption edges. The process of the photon absorption is dominated by the dipole transition, whose intensity $I(h\nu)$ is given by the following formula.

$$I(h\nu) = \sum_f |\langle f|T|i\rangle|^2 \delta(E_i - E_f - h\nu), \tag{2.1}$$

where $h\nu$ is a photon energy of the incident x-ray, T a dipole-transition operator, $|i\rangle$ ($|f\rangle$) and $E_{\rm i}$ ($E_{\rm f}$) the initial (final) state and the corresponding energy of the state, respectively. According to Eq. 2.1, it is clear that the transitions accompanied by a change of the angular momentum by ± 1 can have a main contribution to $I(h\nu)$. Figure 2.1(a) represents an absorption process between the $2p$ and $3d$ states for $3d$ TMs. Due to the strong spin-orbit coupling originating from $2p$ holes created by the photon absorption, total spin and orbital angular momenta themselves are no longer good quantum numbers. Instead, the $2p$ states can be labeled with total angular momentum $J = 1/2$ and $3/2$. Accordingly, an absorption spectrum reveals two major peaks at so-called $L_{2,3}$ ($2p_{1/2,3/2} \rightarrow 3d$) edges as shown in Fig. 2.1(b). The intensity of an experimental background can be expressed by a superposition of two arc-tangents in a common manner [47]. It should be noted that a XAS spectrum at the $L_{2,3}$ edges reflects the electronic structures of the final $3d$ states in the vicinity of the $E_{\rm F}$, because the initial states in the $2p$ core level are well described by atomic orbitals. In the present study, the absorption spectroscopy is operated in the total-electron yield (TEY) mode, which detects drain current from the sample generated by irradiation of the incident soft x-ray. The TEY mode has the potential probing

depth of $\sim$ 5 nm from the surface, which is determined mainly by the mean free path in the energy range of the soft x-ray [48]. Therefore, the measurement in the TEY mode is quite surface-sensitive.

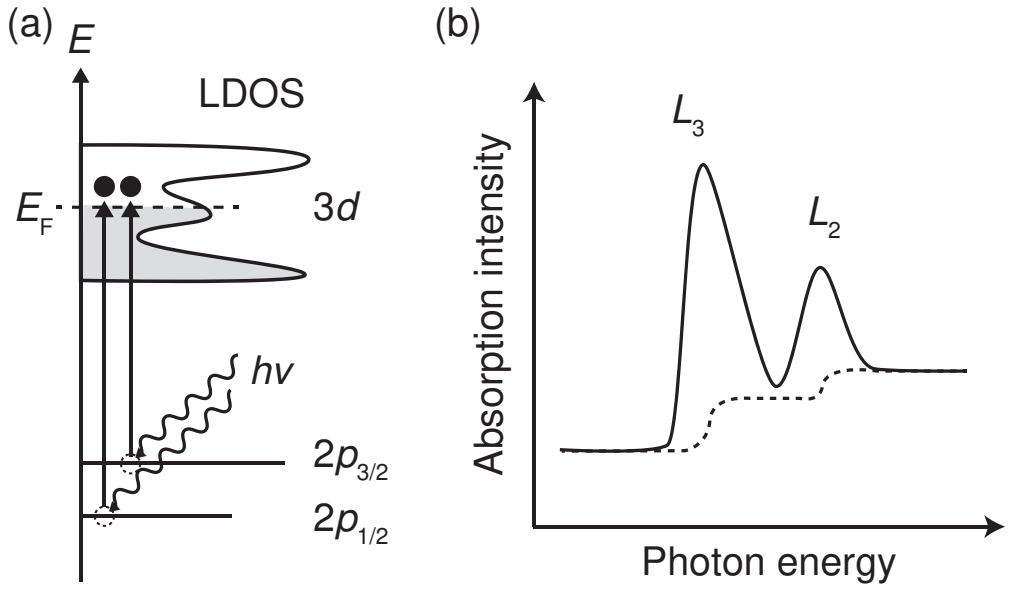

Figure 2.1: Principle of XAS. (a) Schematic diagram of electron excitation from the $2p$ core levels to the $3d$ bands. (b) Typical absorption spectrum at the $L_{2,3}$ edges of $3d$ TMs. A dotted line represents an absorption background.

2.2 X-ray magnetic circular dichroism

Combined with circularly polarized x-ray, the information on the sample magnetism can be extracted from the XAS measurement. For ferromagnetic materials in which the $3d$-band occupation differs depending on the spin channel, the photon absorption process varies with respect to the relative direction between the photon helicity and $3d$ majority spin, as shown in Fig. 2.2(a). This originates from that the right (left)-handed circularly polarized light has the angular momentum of +1 (-1), and then the transition obeys the selection rules. Two absorption spectra toward different circular polarization are distinguished as μ_+ and μ_-, and those difference $\mu_+ - \mu_-$ is defined as x-ray magnetic circular dichroism (XMCD). In Fig. 2.2(b), typical XAS and XMCD spectra at the $L_{2,3}$ edges of $3d$ TMs are presented. The important is that this technique possesses an element specificity, which arises from an element-dependent energy range of absorption edges. Unlike conventional techniques for the characterization of magnetism, this allows us to extract a particular

magnetic component even when measuring a material composed of more than two magnetic elements. Further, by applying XMCD sum rules [49, 50] to the experi-

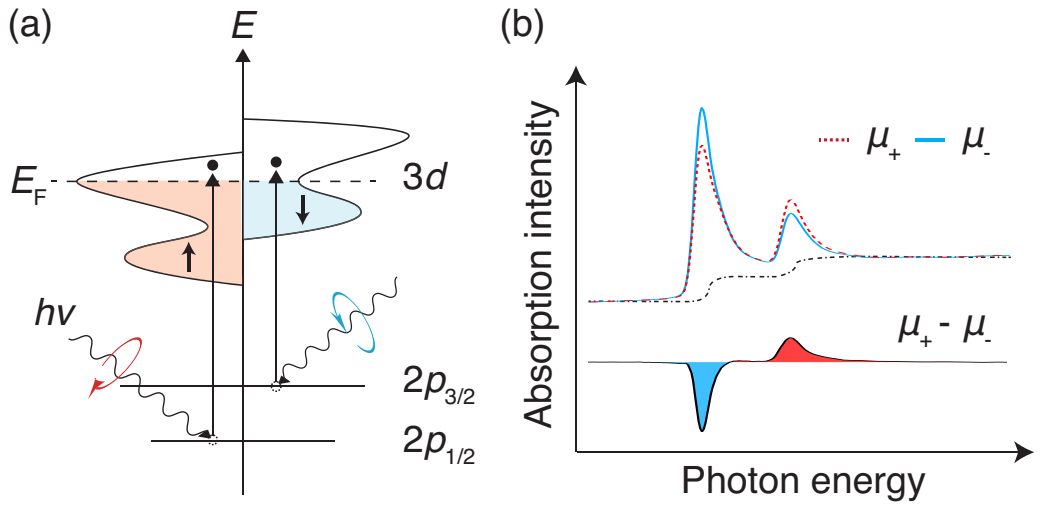

Figure 2.2: Principle of XMCD. (a) Schematic diagram of electron excitation from the $2p$ core levels to the each spin channel of the $3d$ bands. (b) Typical XAS (top) and XMCD (bottom) spectra toward different circularly-polarized lights at the $L_{2,3}$ edges of $3d$ TMs. An absorption background is indicated by a dot-dashed line.

mental XAS and XMCD spectra, we can separately estimate the quantitative values of the spin ($M_{\rm spin}$) and orbital ($M_{\rm orb}$) magnetic moments, according to the following equations.

$$M_{\rm orb} = -\frac{4\int_{L_3+L_2}(\mu_+ - \mu_-)\mathrm{d}\nu}{3\int_{L_3+L_2}(\mu_+ + \mu_-)\mathrm{d}\nu}(10 - n_d), \tag{2.2}$$

$$M_{\rm spin} + 7M_{\rm T} = -\frac{6\int_{L_3}(\mu_+ - \mu_-)\mathrm{d}\nu - 4\int_{L_3+L_2}(\mu_+ - \mu_-)\mathrm{d}\nu}{\int_{L_3+L_2}(\mu_+ + \mu_-)\mathrm{d}\nu}(10 - n_d), \tag{2.3}$$

where integration is conducted with respect to the photon energy $h\nu$ over the L_3 and/or L_2 edges, and n_d is the number of $3d$ electrons. The $M_{\rm T}$ term is related to the magnetic dipole moment, which originates from the anisotropy of $M_{\rm spin}$ [51] and can be neglected when the spectra are measured in the geometry at "magic angle" [52].

2.3 Scanning tunneling microscopy and spectroscopy

2.3.1 Theory of tunneling

The quantum mechanics allows the tunneling of electrons through a potential barrier, even when their energy is lower than the barrier height. The most simplified model is that the electrons pass through a one-dimensional potential barrier (height V_0, width w) as presented in Fig. 2.3. The electrons, coming from Region I and impinging on the potential barrier in Region II, can exist in Region III with a finite probability. A wave function of the electrons $\Psi(\boldsymbol{r})$, whose probability density to be located at a position $\boldsymbol{r}$ corresponds to $|\Psi(\boldsymbol{r})|^2$, obeys the time-independent Schrödinger equation in a stationary limit [53]:

$$\left[-\frac{\hbar^2}{2m}\nabla^2 + V(\boldsymbol{r}) - E\right]\Psi(\boldsymbol{r}) = 0 \tag{2.4}$$

$$V(\boldsymbol{r}) = \begin{cases} V_0 & (\text{Region II}) \\ 0 & (\text{Region I, III}) \end{cases} \tag{2.5}$$

where $\hbar$ is the reduced Planck constant, m the mass of the electron, $V(\boldsymbol{r})$ potential, and E the energy of the electrons. A general solution of this equation is in the following form:

$$\Psi(\boldsymbol{r}) = Ae^{ik\boldsymbol{r}} + Be^{-ik\boldsymbol{r}}, \text{ where } k = \frac{\sqrt{2m|V(\boldsymbol{r}) - E|}}{\hbar}. \tag{2.6}$$

Under boundary conditions at the interface between the regions, the transmission probability T, in proportion to the tunneling current I, can be calculated as

$$T \propto e^{-2\kappa w}, \text{ where } \kappa = \frac{\sqrt{2m|V_0 - E|}}{\hbar}. \tag{2.7}$$

This fast dumping of T through the potential barrier clearly leads to the sensitivity of the STM measurement to a tip-surface distance.

2.3.2 Tersoff-Hamann model

To extract the information on the electronic structures of the sample surface from the STM measurement, it is convenient to make some assumption on the tip state. Within the first-order perturbation theory, I is expressed as follows [54]:

$$\begin{aligned} I &= \frac{2\pi e}{\hbar}\sum_{\mu,\nu}[f(E_\mu)\{1 - f(E_\nu + eV_\mathrm{s})\} - f(E_\nu + eV_\mathrm{s})\{1 - f(E_\mu)\}] \\ &\quad \times |M_{\mu\nu}|^2\delta(E_\mu - E_\nu), \end{aligned} \tag{2.8}$$

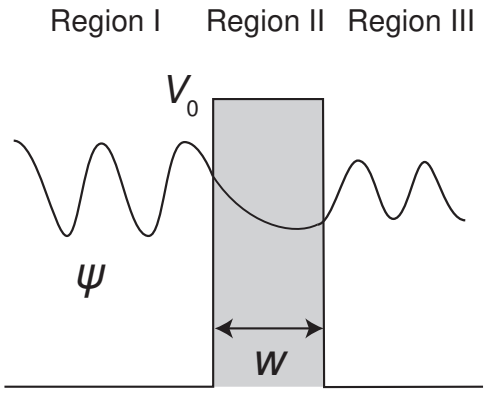

Figure 2.3: Tunneling through the potential. The decay of the electron wave function Ψ via the potential barrier is illustrated.

where $f(E)$ is the Fermi distribution function, $E_{\mu,\nu}$ the energies for wave functions $\Psi_{\mu,\nu}$ of two electrodes, $V_{\rm s}$ bias applied between electrodes. Note that, in the actual STM measurement, one of the electrode corresponds to the tip and the other the sample surface. $M_{\mu,\nu}$ is the tunneling matrix element determined from an overlap between the wave functions Ψ_μ and Ψ_ν. According to the Bardeen's theory [55], its numerical expression is

$$M_{\mu,\nu} = -\frac{\hbar^2}{2m}\int d\boldsymbol{S}\cdot\left(\Psi_\mu^*\boldsymbol{\nabla}\Psi_\nu - \Psi_\nu\boldsymbol{\nabla}\Psi_\mu^*\right), \tag{2.9}$$

where integral is over any surface within the barrier region. Tersoff and Hamann assumed s-type wave functions for the tip, and then $M_{\mu,\nu}$ becomes simply a function of local density of states (LDOS) of the sample [56, 57]. In a low $V_{\rm s}$ limit, I can be a reduced expression of

$$I \propto \int_0^{eV_{\rm s}} \rho_{\rm s}\left(\boldsymbol{r_0}, E\right)\rho_{\rm t}\left(\pm eV_{\rm s} \pm E\right)dE, \tag{2.10}$$

where $\rho_{\rm s}(\boldsymbol{r_0}, E)$ corresponds to the DOS at the position of the tip center $\boldsymbol{r_0}$, and $\rho_{\rm t}$ the DOS of the tip. Here, all the energies are measured with respect to the $E_{\rm F}$. This relationship tells that the sample LDOS integrated to the measurement voltage can be a counterpart of what measured in the STM. Under the WKB approximation [58], the following expression can be obtained:

$$I \propto \int_0^{eV_{\rm s}} \rho_{\rm t}(\pm eV_{\rm s} \mp E)\rho_{\rm s}(E)\cdot T \tag{2.11}$$

$$T \approx \exp\left[-2(s+R)\sqrt{\frac{2m}{\hbar}\left(\frac{\Phi_s+\Phi_t}{2}+\frac{eV_{\rm s}}{2}-E\right)}\right], \tag{2.12}$$

where s is distance of nearest approach, R radius of curvature for a tip apex, and $\Phi_{\rm s}$ ($\Phi_{\rm t}$) a work function of the sample (tip). Within a common approximation of a constant DOS for the tip, the differential conductance $\mathrm{d}I/\mathrm{d}V_{\rm s}$ reflects the sample LDOS.

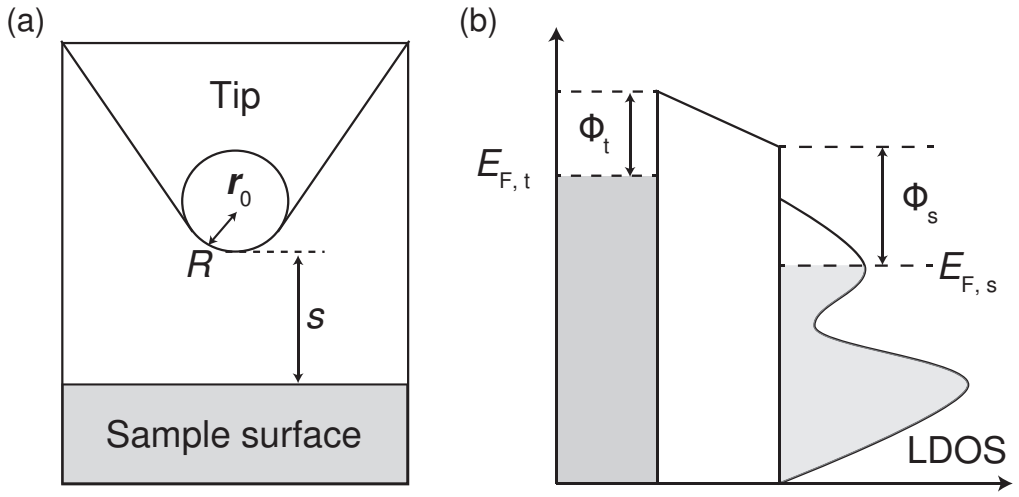

Figure 2.4: Simplified model for the tip. (a) Tip assumed in the Tersoff-Hamann model. The center of the tip, radius of curvature, and nearest approach are labelled with $\boldsymbol{r_0}$, R, and s, respectively. (b) Tunneling model in the STM measurement assuming the constant LDOS of the tip.

Chapter 3

Measurement systems

3.1 STM and preparation chamber

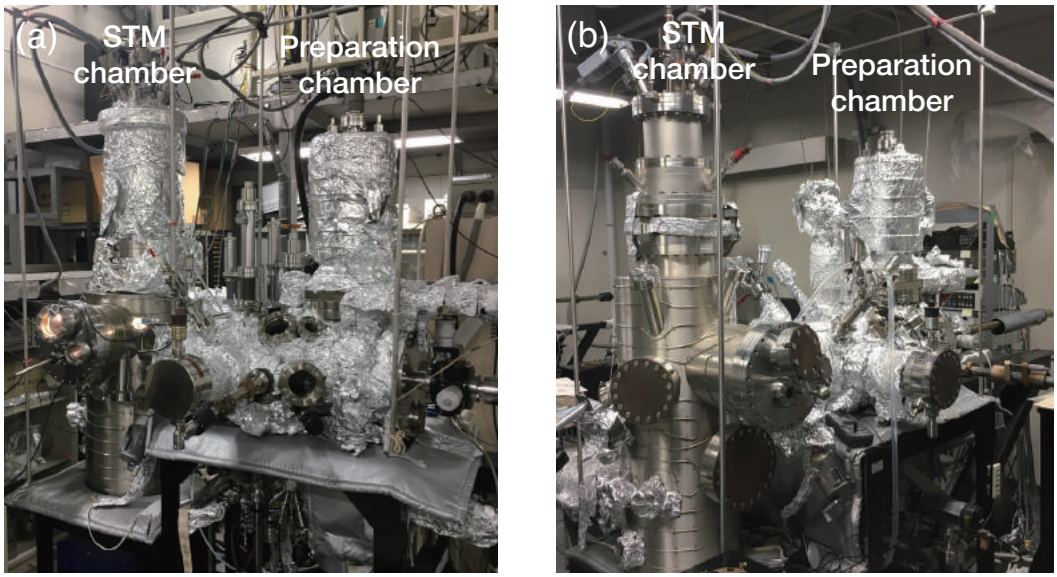

Figure 3.1: UHV-STM apparatuses operated at (a) 4 K and (b) 77 K.

STM measurements were performed under ultrahigh vacuum (UHV) condition ($< 3.0 \times 10^{-11}$ Torr) using Scienta Omicron STM equipped with cryostat, operated at 4 K with LHe cooling [Fig. 3.1(a)] and 77 K with LN_2 one [Fig. 3.1(b)]. A good UHV condition could be achieved by a basic pumping with rotary and turbo-molecular pumps, in combination with ion and titanium-sublimation pumps for a further improvement in pressure. All the processes needed for a sample preparation including a surface cleaning, nitrogen bombardment, iron deposition and subsequent annealing were conducted in the UHV preparation chamber ($< 1.0 \times 10^{-10}$

Torr). The sample grown in the preparation chamber was transferred into the STM chamber without breaking UHV (namely, $in\text{-}situ$ measurement). A sharp tip, made of tungsten wire and chemically etched with sodium hydroxide solution, was used for the STM measurement. The tip apex was cleaned by sputtering with Ar^+ ions and heated by electron bombardment to obtain an acute and stable tip configuration. For the STS measurement, the differential conductance dI/dV was recorded using a conventional lock-in technique with a bias-voltage modulation of several tens mV and 700-900 Hz.

3.2 UVSOR BL 4B

For the element-specific XAS/XMCD measurements, an energy-tunable x-ray emitted from a synchrotron light source is indispensable. Here, all the synchrotron-based measurements were performed using BL 4B at Ultra Violet Synchrotron Orbital Radiation (UVSOR)-Ⅲ, the facility of the Institute for Molecular Science, Okazaki, Japan. This beamline can acquire a high energy resolution of $E/\Delta E > 5000$ in the soft x-ray range, by adopting a varied-line-spacing plane grating monochromator (VLS-PGM) based on the Hetrrick-type design [59, 60] as shown in Fig. 3.2. The degree of circular polarization was ~ 65 % during our experiments, determined by measuring reference ferromagnetic samples. The x-ray propagation vector lay within the $(1\bar{1}0)$ plane of the Cu(001) substrate. A XMCD chamber installed at BL

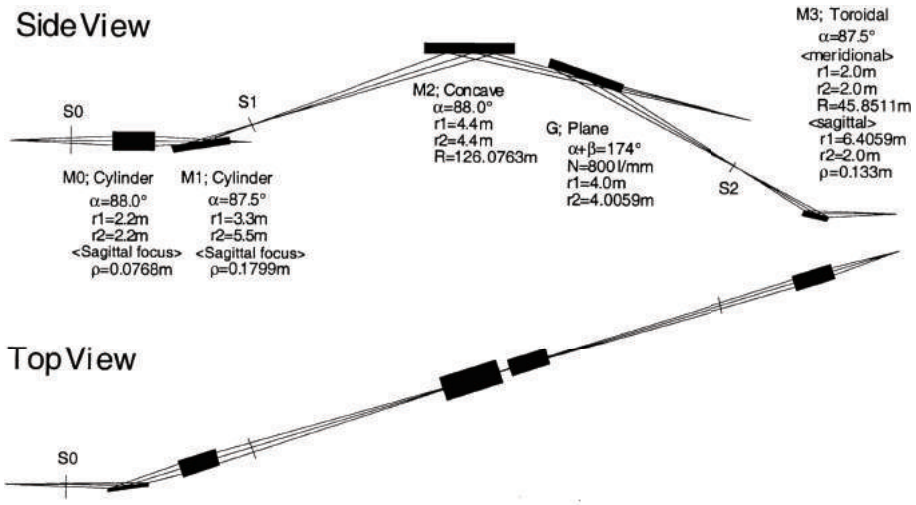

Figure 3.2: Layout of the VLS-PGM beamline BL 4B at UVSOR [59].

4B is presented in Fig. 3.3. The main measurement system is equipped with a split multifilamentary NbTi superconducting magnet [61]. Magnetic field B up to $\pm$ 5 T can be applied to the sample in the direction parallel to an incident x-ray. By

rotating the sample manipulator, we could perform the XMCD measurement in any incidence at an angle θ, where θ is defined as the angle between the sample normal and incident x-ray. For the investigation of magnetic anisotropy, the spectra were recorded mainly in the normal ($\theta = 0°$) and grazing ($\theta = 55°$) incidence. The latter corresponds to the measurement at the magic angle discussed above [52]. The sample was prepared in the UHV preparation chamber connected to the measurement chamber [Fig. 3.3(a)]. An all-in-one sample manipulator is equipped in the preparation chamber, at which all the preparation and characterization can be done without extra transferring. During the annealing of the sample, temperature was monitored with a thermocouple located close to the substrate. The sample surface could be characterized using any of LEED, reflection high-energy electron diffraction, and Auger electron spectroscopy. All the measurements were performed at ~ 8 K with a LHe cooling.

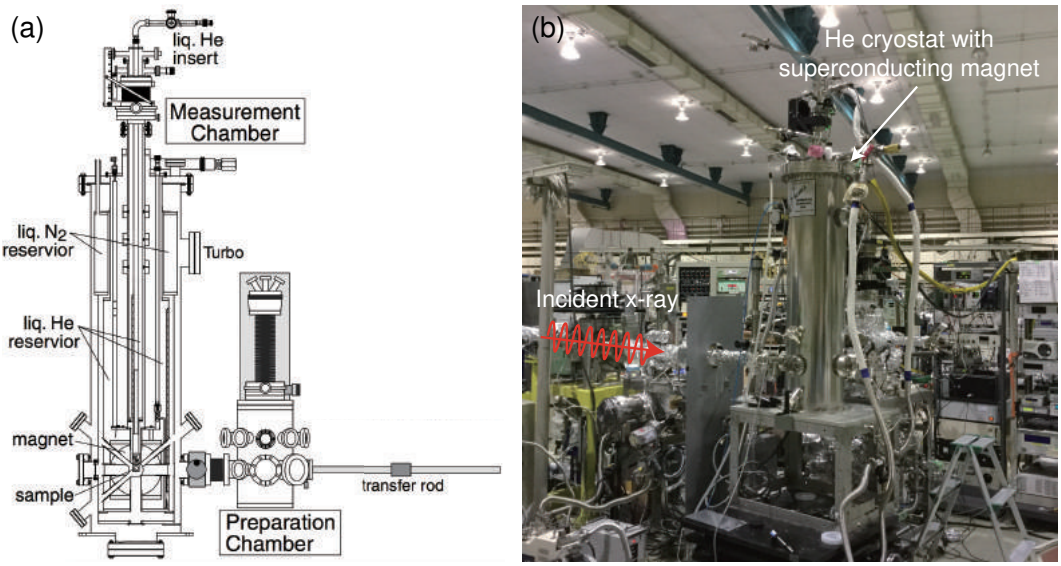

Figure 3.3: XMCD measurement system in BL 4B at UVSOR. Schema (a) and actual view (b) of the system are presented [61].

3.3 Sample preparation

3.3.1 Substrate cleaning

A clean surface of the Cu(001) substrate was prepared in the following steps: First, a single crystal of Cu(001) was chemically etched in a mixed solution of methanol and nitric acid. The cleaned single crystal was mounted on a molybdenum sample holder, fixed with tantalum wires as shown in Fig. 3.4. After introducing the sample

inside the UHV preparation chamber, the cycles of sputtering with Ar^+ ions and subsequent annealing at 800 K were repeated several times. The cleanness of the Cu surface was finally checked by a direct imaging with STM, as well as the sharp spots observed in a LEED pattern.

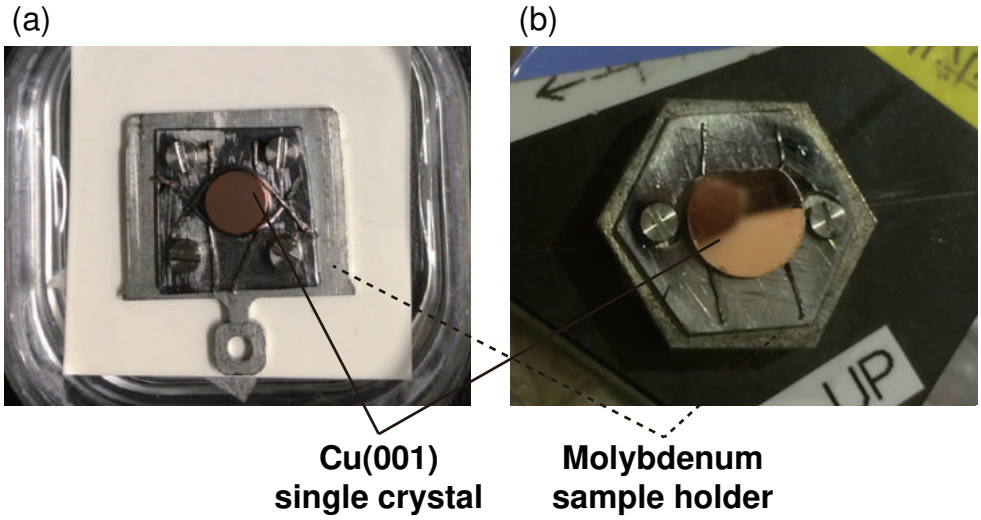

Figure 3.4: Cu(001) single crystal mounted on the (a) STM and (b) XMCD sample holder.

3.3.2 Nitrogen bombardment

Nitrogen ions, with an energy of 0.5 keV, were implanted to the surface by means of bombardment using a commercial ion gun (ULVAC-PHI). The bombardment was conducted under a pressure of $\sim 2.0 \times 10^{-5}$ Torr, typically for 15 min. The ion current could be measured through electrodes touching to the sample holder, so that the amount of the implanted nitrogen ions was checked to be enough to saturate the Cu surface.

3.3.3 Iron deposition

Iron was deposited at room temperature (RT) from a high-purity Fe rod (99.998 %) using an EFM evaporator (FOCUS). Thermal electrons emitted from a tungsten filament inside the evaporator were designed to focus on an Fe rod apex, and heated Fe started to be evaporated with a finite flux monitored by the electronics. The deposition rate was almost the same during every deposition, estimated to be ~ 0.2 ML/min. Note that monolayer was defined with respect to the density of surface Cu atoms of the Cu(001) crystal.

Chapter 4

Orbital-selective tunneling process observed in monolayer Fe_2N on Cu(001)

The contents of this chapter are published in the following:
Y. Takahashi, T. Miyamachi, K. Ienaga, N. Kawamura, A. Ernst, and F. Komori, *Phys. Rev. Lett.* **116**, 056802 (2016)

4.1 Introduction

Scanning tunneling microscopy (STM) is one of the most powerful tools to investigate surface topographic and electronic structures with an atomic resolution. Surface nanostructures are often discussed based on the topographic image. However, its image contrast mainly reflects the electron tunneling processes between the STM tip and the surface orbitals at each position, i.e., local electronic states [57]. As a consequence, the image does not always correspond to the real surface morphology [62, 63]. Systematic changes of the image contrast as a function of the sample-bias voltage V_{s} have been widely interpreted in terms of energy-dependent electronic structures [64–66]. The STM tip-surface distance d is the alternative for the image change. The strength of the STM tip-sample interaction changes at different d, which can occasionally cause the image variation [67, 68]. The d-dependent image change can be also expected for the surface consisted of several orbitals with different decay length of the wave function into the vacuum, e.g. compound systems. In such systems, the image change could be induced by the shift of the dominant surface orbital contributing to the tunneling process at different d, while a certain surface state usually dominates throughout the vacuum region for elemental systems

[69]. The importance of this orbital selective tunneling process on the d-dependent images was suggested for O/Ru(0001), O/Fe(001) and the rutile TiO_2(011)-(2×1) surfaces [70–73]. However, the lack of the strong experimental evidence reinforced by the solid theory still complicates to achieve a common understanding of the impact of the orbital selectivity on the d-dependent imaging.

In this chapter, we also advocate the importance of an in-depth d-dependent STM imaging and spectroscopy to fully characterize the orbital selective tunneling as the origin of the topographic image changes. A monatomic layer of iron nitride (Fe_2N) on Cu(001) with the ferromagnetic Fe_4N stoichiometry [38, 45] is chosen so as to highlight the role of the orbital selectivity. Due to the strong bonding between Fe and N atoms typical for the nitride compounds [74, 75], we expect hybridization-induced non-negligible contributions of s/p orbitals relative to $3d$ orbitals in the local density of states (LDOS), and the robust surface structure against the tip-induced effect, which meets the purposes of this study.

We here show that the topographic image of the Fe_2N layer changed from a dimerized atomic image reflecting the atomic surface structure to a square lattice of atomic-size dots with increasing d. Corresponding systematic d dependence of the tunneling spectra implied the shift in the dominant electronic states contributing to the tunneling process. Combining with the LDOS calculations by first principles, we have attributed these to the change of the dominant orbitals detected by the STM tip from the Fe $3d$ states to the s/p states with increasing the tip-surface distance. The results resolve the discrepancy for the topographic images of the previous STM studies between the $p4g(2 \times 2)$ structure for thick films and the $c(2 \times 2)$ one for atomic-layer films [38, 45].

4.2 Experiment

Monatomic-layer iron nitrides were prepared in ultrahigh vacuum (UHV) with a base pressure of better than 1.0×10^{-10} Torr in the following process. First, a clean surface of Cu(001) was obtained by several cycles of sputtering with Ar^+ ions and subsequent annealing at 820 K. Then, N^+ ions with an energy of 0.5 keV were bombarded to the clean surface and submonolayer Fe was subsequently deposited at room temperature (RT). After annealing at 570 K, well-ordered iron nitrides were obtained on the surface. The surface structure was confirmed by LEED at RT, and STM at 77 K. For the scanning tunneling spectroscopy, the differential conductance dI/dV was recorded using a lock-in technique with a bias-voltage modulation of 20 mV and 719 Hz.

4.3 Results and Discussion

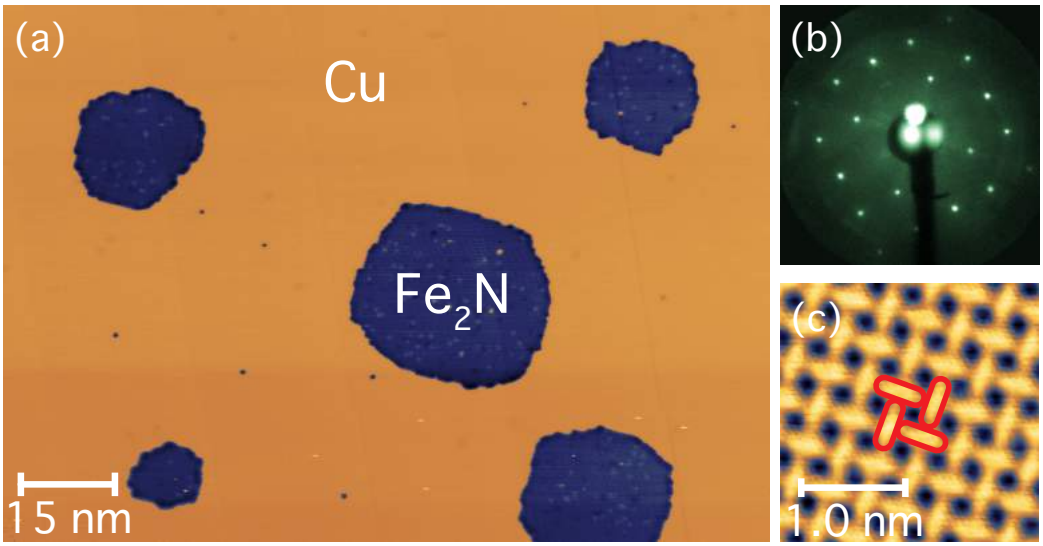

Figure 4.1: (a) Large scale topographic image at $V_s = 100$ mV, $I = 5$ nA. (b) LEED pattern obtained with an incident electron energy of 100 eV. (c) Close view of a topographic image for the Fe_2N islands revealing a dimerization of Fe atoms ($V_s = 50$ mV, $I = 5$ nA). The dimerization is indicated by encirclement.

A large-scale topographic image of the surface is shown in Fig. 4.1(a). Iron-nitride islands of several tens of nanometers in diameter are formed on the Cu(001) surface. A LEED pattern of the same surface shown in Fig. 4.1(b) exhibits the $p4g(2\times2)$ symmetry identical to that of the previous studies [38, 45]. A close view of the STM image shows a dimerized structure as shown in Fig. 4.1(c), which agrees with the LEED pattern. This STM image is similar to that reported by Gallego *et al.* for the thick Fe_4N film [38]. It has been known that, irrespective of the film thickness, the topmost layer of Fe_4N films consists of an Fe_2N single layer [38, 45]. In the surface layer, N atoms occupy the hollow sites of an Fe sublattice. Due to the surface reconstruction, Fe positions are different from those of an ideal Fe_2N layer of the Fe_4N crystal; the Fe atoms are dimerized in the two perpendicular directions, which results in the decrease of the lattice constant compared to the bulk [38, 45]. This surface reconstruction did occur in the films of any thickness as confirmed by LEED. Thus, it still remains unclear why the STM image of the atomic-layer films showed the $c(2\times2)$-like symmetry despite the $p4g(2\times2)$ LEED pattern [45].

To explore the origin of this discrepancy in the previous studies, we first investigated the tunneling-current (I) dependence of the STM images by fixing V_s at 0.25 V. Figure 4.2(a) shows a series of the images with varying I from 0.1 to 45 nA. At $I = 45$ nA, the image consists of distinct Fe dimers. With the decrease of I, the

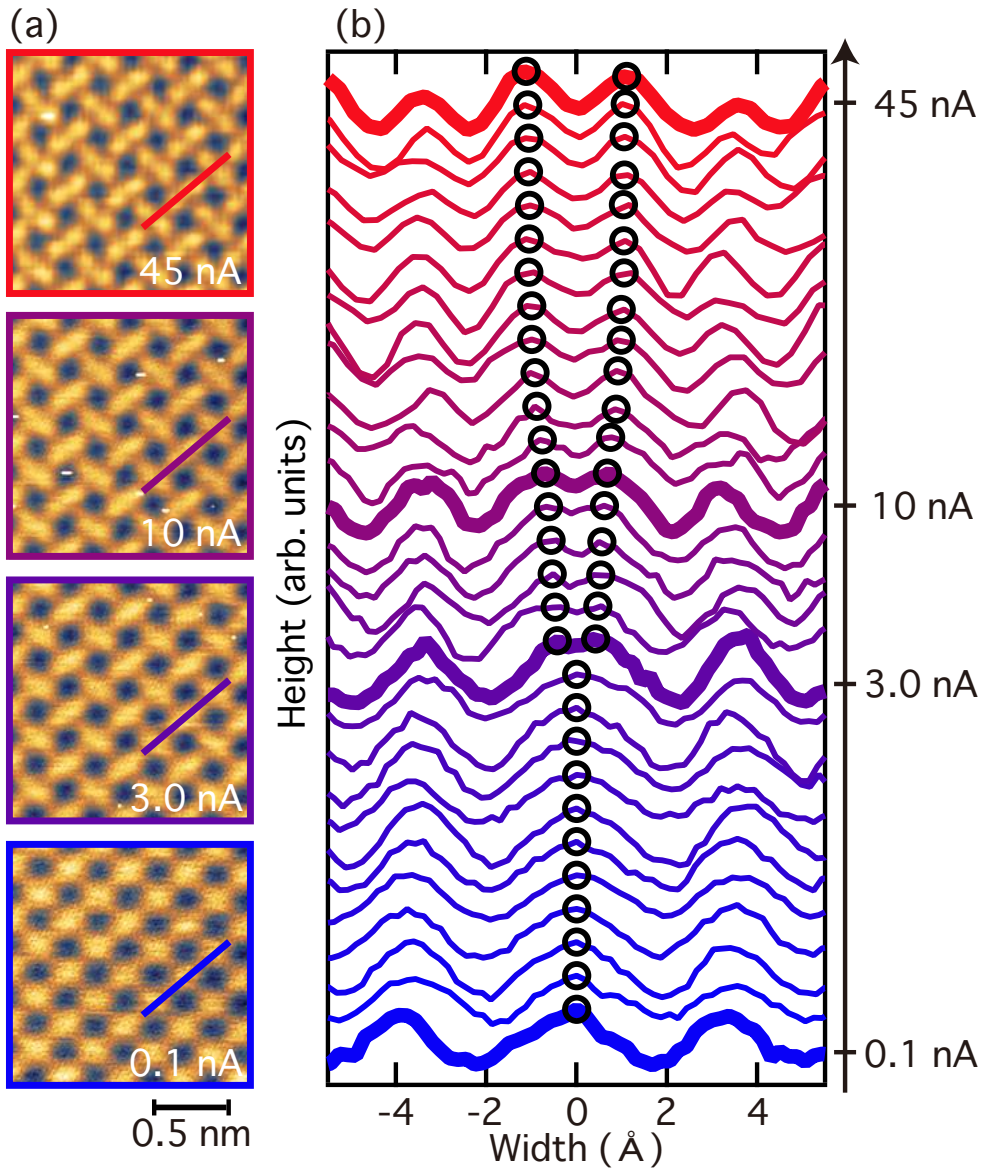

Figure 4.2: Current dependence of STM images. (a) Topographic images taken at $V_s = 0.25$ V with varying I from 0.1, 3.0, 10 to 45 nA. (b) Line profiles at $V_s = 0.25$ V, measured along lines indicated in (a). From the top to the bottom, I varies as follows: 45, 40, 35, 30, 28, 25, 22, 20, 18, 15, 12, 11, 10, 9.0, 8.0, 7.0, 5.0, 3.0, 2.0, 1.0, 0.9, 0.8, 0.7, 0.6, 0.5, 0.4, 0.3, 0.2, and 0.1 nA, respectively. Empty circles indicate peak positions extracted from one Fe dimer.

split of the Fe dimers gradually becomes ambiguous and turns into one elongated structure, similar to that reported by Gallego *et al.* [38]. Finally at $I = 0.1$ nA, the image consists of broad dots, like that reported by Takagi *et al.* [45]. Comparing the structural model with the images for $I \geq 3.0$ nA, we specify that the dots at 0.1 nA are located at the hollow sites of the Fe sublattice with no N atom[1].

For a further grasp of the STM-image change induced by I, we extracted line profiles along the Fe dimer for various I values from 0.1 to 45 nA, as shown in Fig. 4.2(b). One can see that a gradual transformation from a double-peak structure to a single-peak one occurs at around $I = 3.0$ nA with decreasing I[2]. The separation between the two protrusions is almost saturated at $I \geq 20$ nA, and its maximum reaches to 2.23 Å. This length is a little smaller[3] than the reported distance between the dimerized surface Fe atoms of the Fe_2N layer, 2.83 Å of the monatomic-layer Fe_4N determined by LEED I-V [45] and 2.73 Å of the thick Fe_4N film calculated by first principles [38].

It should be noted that the observed I dependence of the Fe-dimer image differs from what generally expected for adjacent two protrusions in the STM observation. A protrusion in the image tends to be broader with increasing d as long as the tip state keeps overlapping the identical states at the surface. Namely, in the present case, the width of the single dot for $I < 3$ nA could be broader than the separation of the two protrusions at higher I if we assumed that the same states at the surface was detected in the entire I range. However, this is not the case in the present observations [4].

To understand the role of the electronic states for the change of STM images, we performed extensive first-principles calculations of the surface LDOS for the monatomic Fe_2N layer on Cu(001) using a self-consistent Green function method within the density functional theory (DFT), specially designed for semi-infinite layered systems [72]. Figure 4.3(a) shows the total, spin- and elementally-resolved LDOS of the Fe_2N surface. Besides large contribution of minority spin states originating from Fe, N majority spin states also contribute to the total LDOS near the Fermi energy (E_F) at the surface. Typical dI/dV spectra recorded above the Fe_2N and Cu(001) are shown in Fig. 4.3(b). In contrast to the Cu spectrum with only minor features, the Fe_2N spectrum shows several peaks located at V_s = -0.35, -0.15, 0.17, 0.52, and 0.79 V, respectively, which well correspond to the peaks of the calculated total LDOS shown in Fig. 4.3(a). Note that, possibly due to the tip condition, the fine structures at the occupied states in the calculation are not so obvious in the

[1] See also Fig. 4.5 and related discussion on the charge distributions calculated at different distances.

[2] This threshold slightly changes depending on the tip condition.

[3] This could be attributed to the difference between an exact atomic position and a projected LDOS distribution of the Fe dimer at each setpoint.

[4] See Appendix A for a numerical simulation of simple broadening of the charge density.

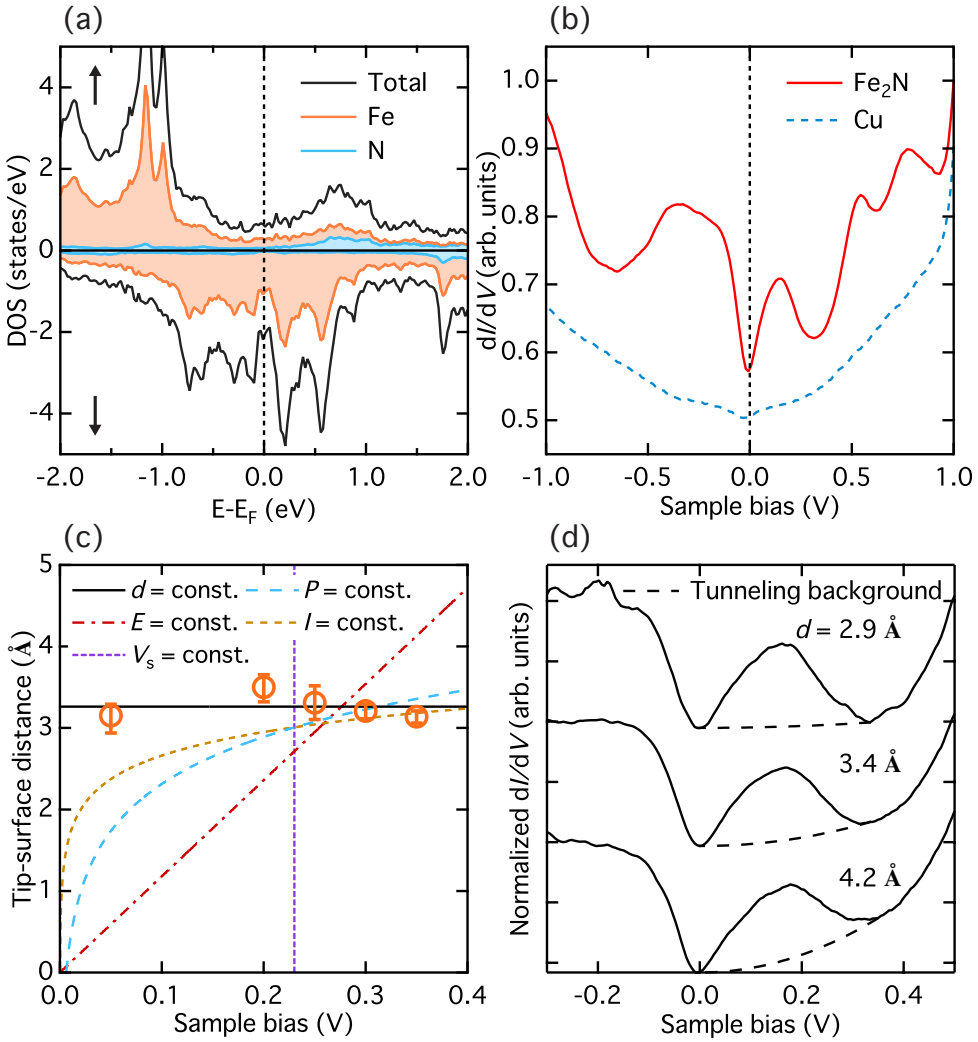

Figure 4.3: (a) Spin-resolved LDOS of single-layer Fe_2N on Cu(001). Fe and N states are separately shown. (b) dI/dV spectra of Fe_2N (solid) and bare Cu (dotted). The STM tip was stabilized at $I = 30$ nA and $V_s = 1$ V. (c) Threshold d_c for the image change. Empty circles indicate parameter sets when the shift in the image from the dimerized to the dot structure occurred. Lines fitted freely to the experimental data with assuming the constant d (solid), E (dot-dashed), V_s (fine-dashed), P (rough-dashed) or I (dashed) in Eq. (4.1) are also indicated. (d) Distant-dependent dI/dV spectra measured at $d = 4.2,\ 3.4,$ and 2.9 Å from the bottom to the top. Dashed curves indicate a tunneling background obtained by a Tersoff-Hamann approximation.

experimental dI/dV spectrum. Thus, hereafter we focus on the unoccupied states (positive sample bias) near the E_{F}.

In the STM measurement, local atomic structures and/or electronic properties of the surface can be modified by the experimental parameters such as I, V_{s}, d, the local Joule heating $P = V_{\mathrm{s}} \times I$, and the electric field $E = V_{\mathrm{s}}/d$ [76]. To elucidate which parameter is crucial to induce the transformation of the STM image in the present study, we have taken the images in various combinations of I and V_{s}. Here, we determine I_{c} and d_{c}, which denote the critical tunneling current and tip-sample distance that the image transforms from the dimerized to the dot structure, respectively. The d_{c} was evaluated from I_{c} at each V_{s} by applying Simmons' rule [77]

$$d_{\mathrm{c}} = -\frac{\hbar}{2\sqrt{2m\Phi}} \ln\left(\frac{R_0 I_{\mathrm{c}}}{V_{\mathrm{s}}}\right), \tag{4.1}$$

where m is the electron mass, Φ an average work function of the tip and the sample, and R_0 the resistance for a single-atomic point contact of 12.9 kΩ [78]. An average Φ value of 5.5 eV, obtained from the fitting of several experimental I-d curves is used in the evaluation[5]. Figure 4.3(c) shows a plot of d_{c} as a function of V_{s} (empty circles). The nearly constant d_{c} values of 3.3 Å (solid line) are found, suggesting that I_{c} increases (decreases) at higher (lower) V_{s}, and the image change is entirely caused by d. None of E, V_{s}, P and I can be a threshold for the image change. Therefore, we can conclude that the observed image change is triggered by the tip-surface distance[6].

It has been known that the decay length of the wave function strongly depends on an orbital character, i.e., the $3d$ states decay into the vacuum faster than the s/p states [79]. The different decay lengths between the d and s/p states were previously investigated and confirmed in terms of the spin polarization [80, 81]. Thus, the states detected by the tip with smaller distance could have more Fe $3d$ character.

To confirm this, we measured dI/dV spectra with various d values as shown in Fig. 4.3(d). Here, the tip was fixed at $V_{\mathrm{s}} = 0.1\ V$, and all the spectra are normalized to the intensity at $V_{\mathrm{s}} = -0.1$ V. Note that the corresponding STM images at $d = 2.9, 3.4$ and 4.2 Å consist of the distinct, blurred dimerized structures and the dot structure, respectively. At $d = 2.9$ Å, the background contribution is small and the peak around 0.2 V is mainly attributed to the Fe $3d$ state, in comparison with the theoretical calculations (see Fig. 4.3(a). A detailed orbital assignment is discussed below). However, one can clearly see that the contribution of an integrated background signal monotonously increases as the tip becomes far. It should

[5] See Appendix B for the nearly constant Φ values with respect to the tip-surface distance.

[6] The observed LEED pattern agrees with the STM image at short d. Therefore, the tip-sample interaction is excluded as the origin of the image change in the present case.

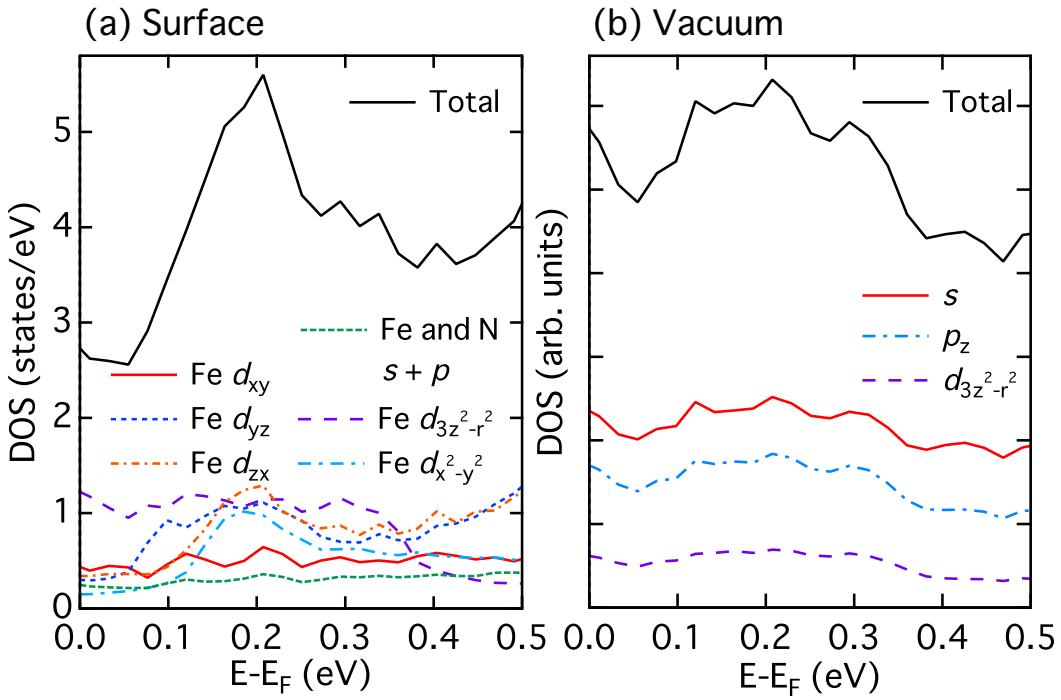

Figure 4.4: Total and orbital-resolved LDOS of (a) surface and (b) vacuum (4 Å above the surface) layers. The states with negligible intensity in this energy range are not shown here. In the vacuum layer, LDOS cannot be separated into each atomic component due to a strong orbital mixing between Fe and N.

be noted that an exponential background signal is mainly due to the tunneling processes between the tip states and the sample s/p states [58, 79]. Therefore, a series of the d-dependent dI/dV spectra well supports our interpretation on the observed d-dependent change of the STM image. Namely, at short d, the tunneling process through the Fe $3d$ states dominates that through the s/p states, and it results in the STM image of the dimerized structure.

We have further studied the decay of orbital-resolved LDOS into the vacuum by first-principles calculations to understand the tunneling process in detail. In Figs. 4.4(a) and 4.4(b), we extract dominant orbitals contributing to the total LDOS near the E_{F}. At the surface, the LDOS mainly consists of the Fe $3d$ states and the s/p states are minute as shown in Fig. 4.4(a). It means that, at a short tip-surface distance, the possible states dominantly detected by the STM tip are $3d_{3z^2-r^2}$, $3d_{zx}$ and $3d_{yz}$. Another intriguing is that among $3d$ states, the d_{xy} state shows no clear LDOS around $E - E_{\mathrm{F}} = 0.2$ eV. This indicates a strong hybridization between Fe and N atoms, which leads to delocalization of the d_{xy} state while the other $3d$ states relatively remain localized.

The situation drastically changed in the vacuum layer 4 Å above the surface.

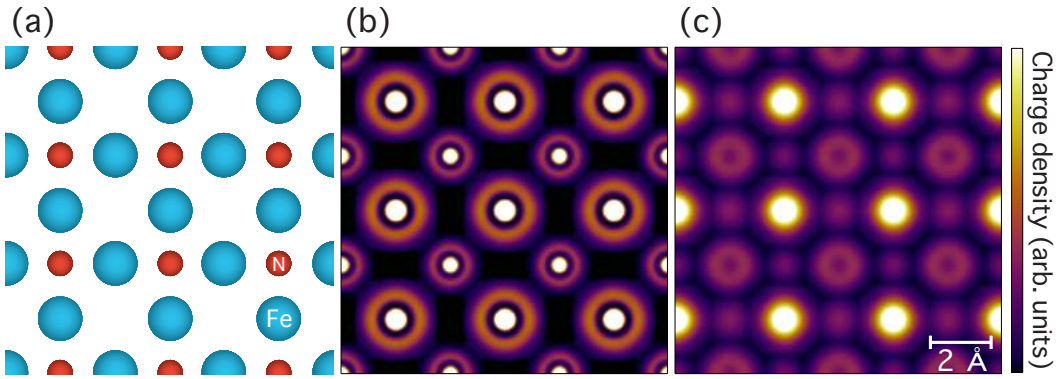

Figure 4.5: Charge distributions calculated at different distances. (a) Unreconstructed $c(2\times2)$ surface model used for the calculation. Large (small) spheres correspond to the surface Fe (N) atoms. (b,c) Charge distribution at d = 1.8 Å (b) and d = 6.5 Å (c).

In Fig. 4.4(b), one can see that the contributions of isotropic s and out-of-plane-oriented p_z overwhelm those of $3d$ except for $3d_{3z^2-r^2}$. This is clearly due to the longer decay lengths of the s/p states than the d states. Such large s/p contributions relative to the $3d$ ones and thus the tip-surface distance dependence of the STM image have not been expected in elemental $3d$ systems, where the surface states mainly of $d_{3z^2-r^2}$ character slowly decay into the vacuum [69]. The considerable enhancement of the s/p contribution in the present case is caused by strong hybridization of N s/p states with Fe s, p, d states, which is characteristic of compound systems.

Finally, we confirm how this shift in the s/p and d contributions at different distances shows up in a spatial distribution of the charge density using DFT. Figure 4.5 shows the calculated charge distributions of states at the energy $E = E_F + 0.25$ eV, corresponding to our experimental V_s of 0.25 V. It should be noted that an energy resolved charge distribution can be associated with STM topographic images within the Tersoff-Hamann model [57]. An unreconstructed $c(2\times2)$ surface shown in Fig. 4.5(a) was used in the calculation for simplicity, instead of the reconstructed $p4g(2\times2)$ one. Thus obtained charge distributions at d = 1.8 Å and 6.5 Å are shown in Fig. 4.5(b) and 4.5(c), respectively[7]. At a shorter distance of 1.8 Å, the charge intensity is high on top of the Fe atoms, because of a large contribution of the Fe $3d$ states. This is consistent with that the surface Fe atoms were distinctly imaged at higher Is [see Fig. 4.2(a)]. In the case of d = 6.5 Å, in contrast, the intensity maxima locate above the hollow site of the Fe sublattice without N atoms. This originates from the dominance of states with s/p characters at larger distances, and

[7]Note that the distances of the calculation cannot be directly compared with the experiments since DFT has less accuracy for reproducing the surface excess charge.

well reproduces the experimental I dependence of the STM images.

4.4 Conclusion

In summary, we have performed the comprehensive STM work to elucidate the origin of the image changes for the monatomic-layer iron nitride on Cu(001). Systematic d-dependent STM imaging and spectroscopy reveal that the observed image change is attributed to the orbital-dependent decay length of the wave function at the surface. The validity of the experimental results is confirmed by the first-principles calculations, which successfully reproduce that the STM image is dominated by the Fe $3d$ states at short distance whereas by the s/p states at long distance. Since the orbital-selective tunneling process is inherent in any STM measurements, the atomic morphology based on the topographic image should be carefully discussed, especially in the compound systems.

Chapter 5

Impact of atomic defects on the macroscopic ferromagnetism of monolayer Fe_2N on Cu(001)

5.1 Introduction

Two dimensional (2D) materials have received much attention due to unique physics absent in higher dimensions [82, 83]. The nature of 2D systems is such a close interplay between structure and electronic states that a small structural perturbation can dramatically alter physical properties. Engineering structural defects is one of the most common ways to add novel functionalities to the 2D materials [84–88]. At the same time, some intrinsic structural defects have been reported to deteriorate ideal properties of the system [89–91]. A large variation in a defect type requires nearly material-by-material observations to elucidate the role of such defects in the physical properties of the 2D system [92–94]. By analogy, the significant impact of the structural defects is expected on magnetic states realized via 2D network of atomic/spin structures, namely in 2D ferromagnets with long-range order or itinerancy. However, due to difficulty in controlling and characterizing the structural defects of atomic-layer ferromagnets, the relationship between a structural disorder and electronic/magnetic states of the system has remained elusive in an atomic-layer limit.

Here, we investigate the impact of atomic point defects on the sample electronic and magnetic properties of a monolayer ferromagnet of Fe_2N on Cu(001). The topography, electronic structures, and magnetic moments of the samples were investigated by scanning tunneling microscopy/spectroscopy (STM/STS) and x-ray absorption spectroscopy/magnetic circular dichroism (XAS/XMCD). This combination of measurement techniques is so useful especially in an atomic-layer limit that the information obtained using microscopic and macroscopic observations comple-

ments each other [95, 96]. Simultaneous STM/STS observations with an atomic resolution revealed the modulation of the electronic structures in a large area around the atomic defects. The present results demonstrate an extensive deterioration of 2D ferromagnetism caused by a small amount of a structural disorder in an atomic scale, which cannot be characterized by macroscopic structural characterizations.

5.2 Experiment

The monolayer Fe_2N samples were prepared under ultrahigh vacuum (UHV) condition ($\leq 1.0 \times 10^{-10}$ Torr) as follows [97]: First, a clean Cu(001) surface was obtained by a repetition of sputtering with Ar^+ ions and subsequent annealing at 820 K. The surface was then bombarded by N^+ ions with an energy of 0.5 keV. The following 1-2 ML Fe deposition was conducted at room temperature (RT), using an electron bombardment type evaporator (EFM, FOCUS) equipped with a high-purity Fe rod (99.998 %). Annealed at 540-570 K, a Cu(001) surface was covered with monolayer Fe_2N, identical to an Fe_2N plane of a $\gamma\prime$-Fe_4N unit cell in which one N atom occupies a hollow site of a fcc Fe lattice [98]. The STM measurements were performed at 4.7 K in UHV ($\leq 3.0 \times 10^{-11}$ Torr) using electrochemically etched W tips. For the STS measurements, the differential conductance $\mathrm{d}I/\mathrm{d}V$ was recorded using a lock-in technique with a bias-voltage modulation of 20 mV and 810 Hz. The XAS and XMCD measurements were performed at BL 4B of UVSOR-Ⅲ in the total electron yield (TEY) mode [59, 61]. The degree of circular polarization was estimated to be $\sim 65\ \%$, and the x-ray propagation vector lay in the $(1\bar{1}0)$ plane of a Cu substrate. All the spectra were recorded at $\sim\ 8$ K and $B = \pm 5$ T applied parallel to the incident x-ray. The symmetry of a surface structure was also checked by low energy electron diffraction (LEED) in each apparatus.

5.3 Results and Discussion

Topographic images of the monolayer Fe_2N samples, prepared by an initial 1 ML Fe deposition and subsequent annealing at different temperatures, are shown in Fig. 5.1(a) to 5.1(c). At the lowest annealing temperature of 540 K [Fig. 5.1(a)], the surface is mostly covered with the monolayer Fe_2N. It is known that an ordered monolayer Fe_2N on Cu(001) is reconstructed into $p4g(2 \times 2)$ symmetry, in which Fe atoms dimerize in mutually perpendicular directions as shown in Fig. 5.1(h) [97]. Therefore, Fig. 5.1(d), a close view of an iron-nitride surface shown in Fig. 5.1(a), suggests that a large fraction of the surface Fe atoms does not form the

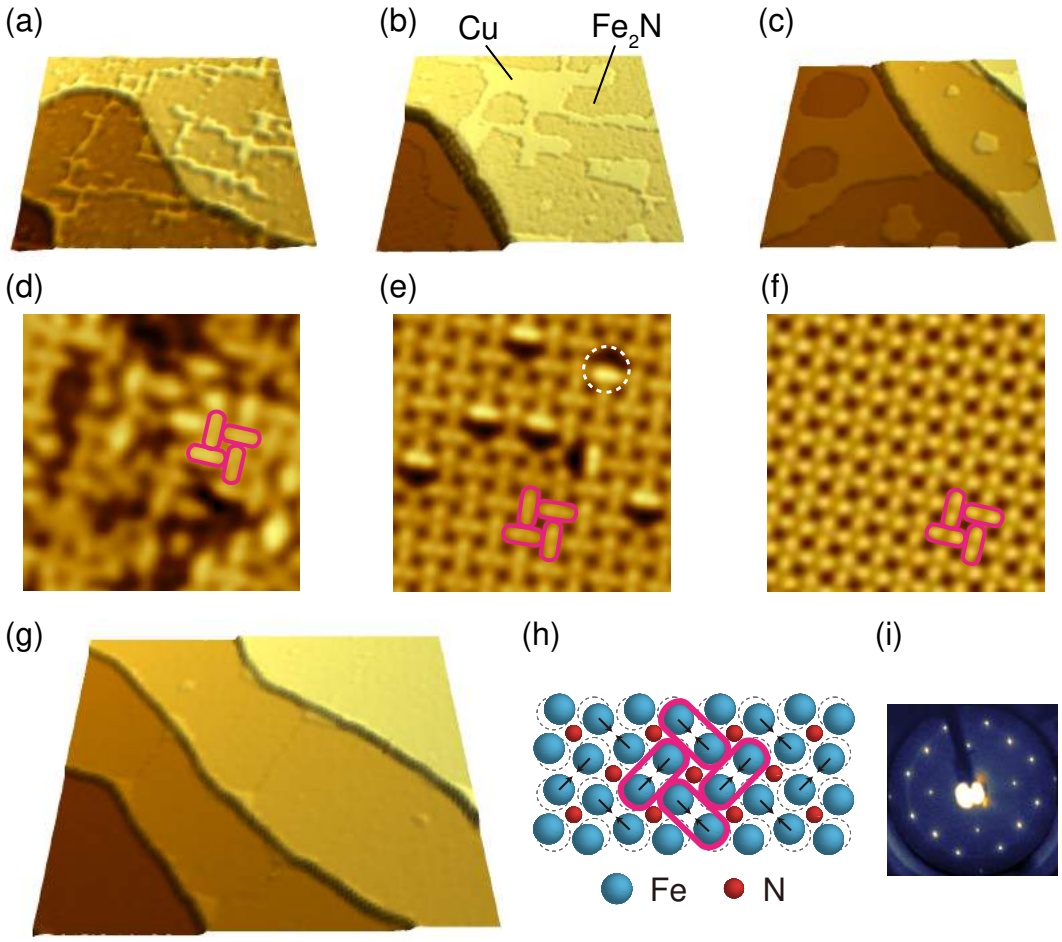

Figure 5.1: Topography of the monolayer Fe_2N on Cu(001). (a,b,c) Topographic images (75×75 nm^2) of the samples prepared by an initial 1 ML Fe deposition and subsequent annealing at (a) 540 K (b) 555 K and (c) 570 K. (d,e,f) Close view (3.5×3.5 nm^2) of the Fe_2N surface for (a), (b), and (c), respectively. The dimerization of the Fe atoms is indicated by encirclement. In (e), the unit of the disordered area is defined by a dotted circle (see text). (g) Topographic image (100×100 nm^2) of the sample grown by an initial 2 ML Fe deposition and annealing at 570 K. The images were taken at (sample bias V_s, tunneling current I) = ($+1.0$ V, 50 pA), (-0.35 V, 0.6 nA), ($+0.1$ V, 20 pA), ($+0.1$ V, 30 nA), ($+0.1$ V, 40 nA), ($+50$ mV, 40 nA), and (-0.1 V, 0.1 nA) for (a), (b), (c), (d), (e), (f), and (g), respectively. (h) Illustration of $p4g(2\times2)$ reconstruction in the surface Fe_2N layer of γ'-Fe_4N. Arrows represent the shift of Fe atoms from an unreconstructed $c(2\times2)$ coordination indicated by dotted circles. Large (small) spheres represent Fe (N) atoms. (i) LEED pattern of the surface shown in (g) obtained with an incident electron energy of 103 eV.

ordered Fe_2N and/or exists without any bond to N atoms. With increase in the annealing temperature up to 555 K, the coverage of an Fe_2N area decreases to 0.65 ML as shown in Fig. 5.1(b). On the other hand, most of the surface Fe_2N possesses well lattice ordering as presented in Fig. 5.1(e). However, the surface contains a small number of point defects recognized as dark holes in the image (identified as missing-Fe defects later). This suggests that the annealing temperature is still low to form the perfectly ordered Fe_2N all over the surface. Eventually, it turned out that an annealing temperature of 570 K was needed for preparing a nearly defectless Fe_2N surface as shown in Fig. 5.1(f). Meanwhile, a further decrease in the coverage of the surface Fe_2N to 0.5 ML can be seen in Fig. 5.1(c). This means that the formation of the highly-ordered Fe_2N was always accompanied by an inevitable loss of initially deposited Fe and/or N atoms during the annealing process.

As a result, the sample almost fully covered with the ordered monolayer Fe_2N could be grown by an initial 2 ML Fe deposition and subsequent annealing at 570 K, as shown in Fig. 5.1(g). The almost 1 ML coverage of the surface Fe_2N was confirmed by a XAS edge jump value at the Fe L ($2p \rightarrow 3d$) edge, normalized by that at the Cu one, of ~ 0.12. A LEED pattern of the surface presented in Fig. 5.1(i) exhibits sharp diffraction spots with the $p4g(2\times2)$ symmetry, indicating a uniform formation of the surface-reconstructed Fe_2N. It should be emphasized that these annealing temperature dependence of the surface lattice ordering was difficult to distinguish by conventional LEED observations; neither symmetry nor sharpness of the spots changed apparently between the samples.

Here, we discuss the relationship between the amount of the initially-deposited Fe and the coverage of the monolayer Fe_2N finally obtained at the surface. The samples shown in Fig. 5.1(a) and 5.1(g) showed similar values of the normalized Fe L edge jump of 0.11 ± 0.01. In principle, the value of the XAS edge jump in a thin-film limit is proportional to the amount of surface/subsurface atoms related to absorption. Therefore, the observed edge-jump values suggest that the coverage of the highly-ordered monolayer Fe_2N was about half the amount of the initially-deposited Fe. The other half was not detected in the edge-jump spectrum after the annealing at 570 K, and thus considered to be buried into the Cu substrate at least outside the XAS probing depth of several nms in the TEY mode [99].

The sample ferromagnetism turned out to be largely affected by the degree of the surface lattice ordering, from the XMCD measurements on on different monolayer Fe_2N samples prepared as follows: After the nitrogen bombardment to the clean Cu(001) surface, three samples were grown by (1.0 ML Fe deposition, subsequent annealing at 540 K), (1.8 ML, 555 K), and (2.0 ML, 570 K). The obtained surfaces were thus almost fully covered by the monolayer Fe_2N with the lattice ordering similar to that shown in Fig. 5.1(d), Fig. 5.1(e), and Fig. 5.1(f), respectively. For convenience, we call them less-ordered, atomic-defect, and highly-ordered sam-

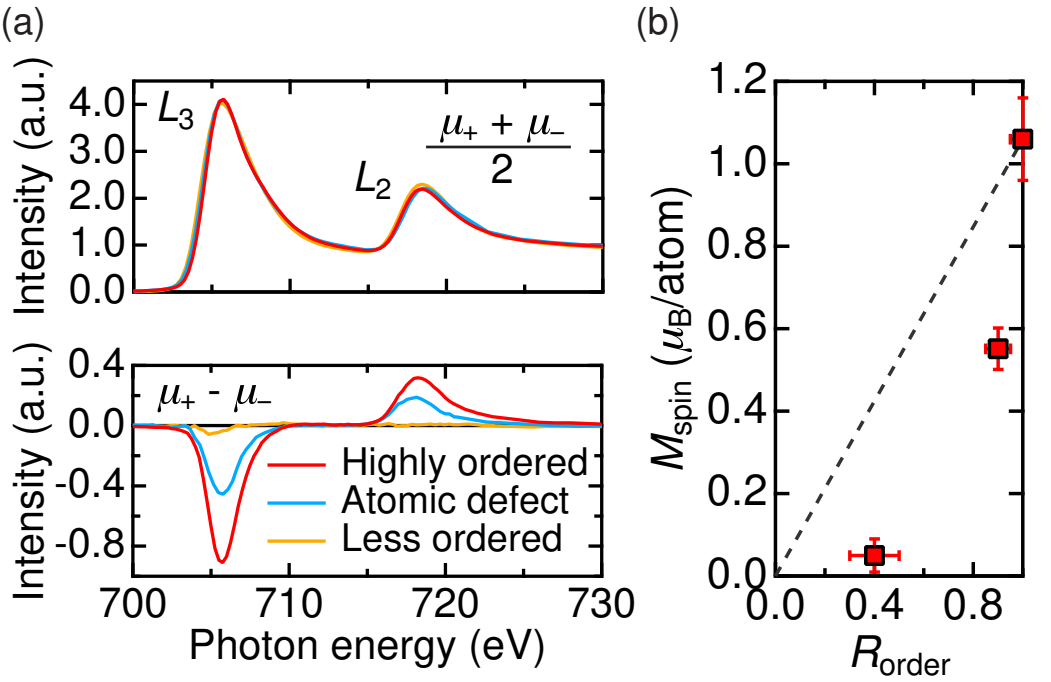

Figure 5.2: Ferromagnetism of the monolayer Fe_2N on Cu(001) with different lattice ordering. (a) Averaged XAS (top) and corresponding XMCD (bottom) spectra of the highly-ordered (red), atomic-defect (blue), and less-ordered (yellow) samples. The spectral intensity is normalized to the Fe L-edge XAS jump. (b) Dependence of M_{spin} values on the area ratio of the $p4g(2 \times 2)$-reconstructed Fe_2N at the surface R_{order}. A dotted line is the fit assuming the decrease in M_{spin} to be a linear of the R_{order}.

ples in that order. Note that the 1 ML coverage of each sample was checked by the normalized Fe L-edge jump values of 0.11 ± 0.01.

Figure 5.2(a) shows averaged XAS $[(\mu_+ + \mu_-)/2]$ and XMCD $(\mu_+ - \mu_-)$ spectra of those samples measured at the Fe $L_{2,3}$ ($2p_{1/2,3/2} \rightarrow 3d$) edges in the grazing incidence ($\theta = 55°$), which mainly reflects magnetic moments along an in-plane easy magnetization direction [98]. Here, μ_+ (μ_-) denotes a x-ray absorption spectrum with the photon helicity parallel (antiparallel) to the Fe $3d$ majority spin, and an incident angle θ is defined as that between the sample normal and the incident x-ray. A nearly identical shape of the XAS spectra between the samples indicates a small variation in the hole coordination of unoccupied $3d$ states. This is in consistent with the STS spectra recorded on each surface shown in Fig. 5.3(b), revealing less variation in a spectral shape between the surfaces on the positive V_{s} side.

Meanwhile, the XMCD intensity clearly decreases as the surface lattice ordering lowers. By applying XMCD sum rules [49, 50] to the obtained spectra, the difference in the spin magnetic moment (M_{spin}) for the Fe atoms can be visible as shown in Fig. 5.2(c), against the ratio of the ordered Fe_2N area R_{order}. Here, the

$R_{\rm order}$ value simply represents the area ratio that the $p4g(2\times2)$-reconstructed Fe_2N occupies the entire surface. For the atomic-defect sample, e.g., the $R_{\rm order}$ value is estimated to be ~ 0.90 by considering 10 % of the disordered area as defined in Fig. 5.1(e). Accordingly, the $R_{\rm order}$ of the less-ordered and highly-ordered samples are estimated to be ~ 0.40 and 1.0, respectively. Note that in the present sum-rule analysis, we used the average number of $3d$ holes ($n_{\rm hole}$) of 3.2, obtained by comparing the area of the experimental XAS spectra with that of a reference spectrum for bcc Fe/Cu(001) with $n_{\rm hole} = 3.4$ [47].

The $M_{\rm spin}$ value of 1.1 $\mu_{\rm B}$/atom for the highly-ordered sample is in good agreement with that calculated by first principles [98]. This ensures that the highly-ordered sample forms an ideal lattice of the reconstructed Fe_2N. The surprising is the $M_{\rm spin}$ value of 0.6 $\mu_{\rm B}$/atom for the atomic-defect sample, almost half the value of the highly-ordered one regardless of the high $R_{\rm order}$ of 0.9. Further decrease of the $R_{\rm order}$ for the less-ordered sample results in much smaller $M_{\rm spin}$ value of ~ 0.05 $\mu_{\rm B}$/atom. The observed non-linear dependence of the $M_{\rm spin}$ values on the $R_{\rm order}$ suggests that the decrease in the $M_{\rm spin}$ cannot be explained assuming only the structurally disordered area is magnetically weak compared to the defect-free Fe_2N. In other words, the lattice disorder should not only cause a small magnetic moment inside the disordered area, but also deteriorate the ferromagnetism of the neighboring, highly-ordered Fe_2N.

To reveal a possible impact of the lattice disorder on the surrounding electronic structures, atomically-resolved STS observations were conducted around the atomic defect shown in Fig. 5.3(a). In comparison with an atomic structural model, one Fe atom is missing atop the defect. It is also obvious that Fe dimers located just below the defects become brighter in the image, indicating the change in the electronic states rather than atomic structure accompanied by defect creation. Hereafter, we call this bright Fe dimer as a protrusion, and a dI/dV spectrum (height profile) recorded above a defect-free Fe_2N surface as a normal spectrum (profile). The dI/dV spectra measured on top of the defect (blue) and the protrusion (red) are shown in Fig. 5.3(b), in comparison with the normal spectrum (black). The spectrum recorded on the defect has high dI/dV intensity at $V_{\rm s} < -0.4$ V compared to the normal spectrum. This can be attributed to a broadening of the peak located at $V_{\rm s} = -0.32$ V, mainly composed of Fe local density of states (LDOS) with d orbitals except for $d_{\rm x^2-y^2}$ [97]. For the spectrum recorded above the protrusion, the peak intensity at $V_{\rm s} = -0.32$ V is lower than that of the normal spectrum. This indicates the intensity decrease in Fe LDOS near the Fermi energy. These changes in the electronic states could lead small magnetic moments of the Fe atoms within the defect/protrusion area, compared to those in the defect-free Fe_2N surface [100].

In the vicinity of the protrusion, the modulation in the electronic structures of the ordered Fe_2N was clearly observed as shown in Fig. 5.3(c), which displays both

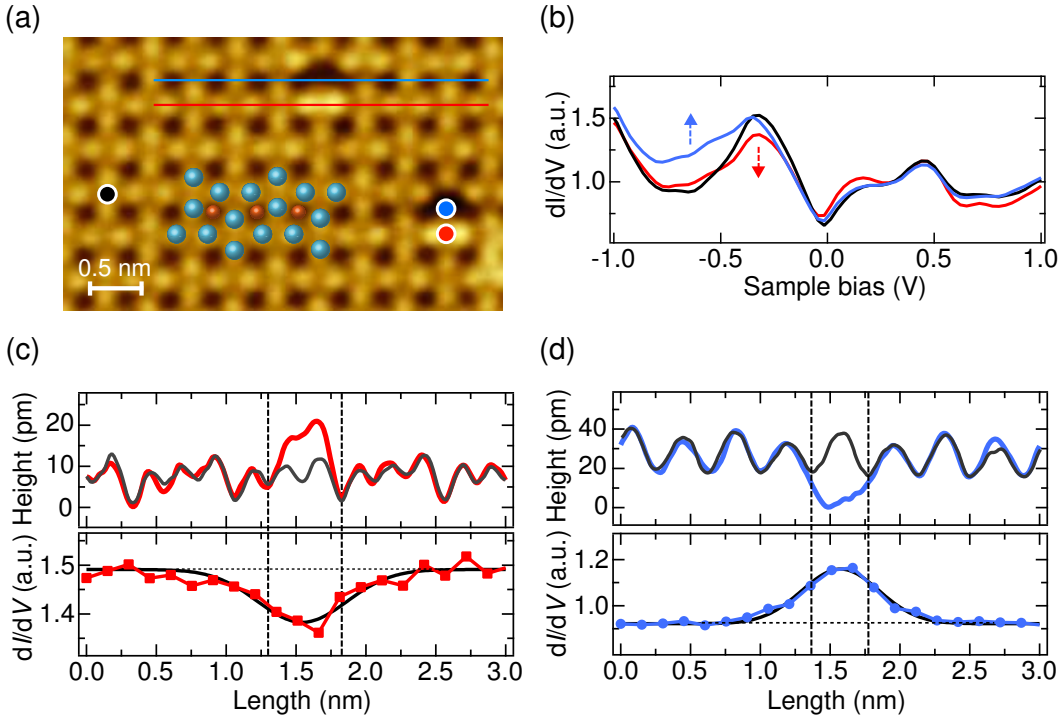

Figure 5.3: Electronic-structure modulation around the atomic defect. (a) Atomically-resolved image of an Fe_2N surface of the atomic-defect sample. Surface Fe (N) atoms are presented by large (small) spheres. (b) dI/dV spectra recorded on the positions of the corresponding colored circles indicated in (a). The tip was fixed at $V_s = +1.5$ V and $I = 5.0$ nA. (c,d) Top: Height profile taken along the (c) red and (d) blue lines shown in (a). Black profiles were measured along the corresponding lines on a defect-free Fe_2N surface. Bottom: dI/dV profile at $V_s = -0.32$ $[-0.65]$ V along the (c) red [(d) blue] line indicated in (a). Details are explained in the text. Solid curves are the fitting of each profile to the Gaussian function.

height and dI/dV profiles across the protrusion. Note that the dI/dV profiles were obtained by first recording point-by-point dI/dV spectra along presented lines, and then plotting the difference in the dI/dV intensity at a specific V_s with respect to the normal spectrum. The structural width of the protrusion, tentatively defined as the length within which its height profile differs from the normal one, is estimated to be 0.5 nm. Meanwhile, the dI/dV profile indicates that the modulation of the electronic structures spreads up to 1.3 nm (the value of 4σ, where σ is the standard deviation of the fitted Gaussian function) across the protrusion. This demonstrates the propagation of the electronic-structure modulation outside the protrusion, about three times wider than its width. A similar discussion can be applied to the point defect: the electronic structures across the defect are modulated over 1.1 nm, almost three times wider than the defect size of 0.4 nm as shown in Fig. 5.3(d). Note that, also in a vertical direction from a defect center to the top/bottom of Fig. 5.3(a), the

electronic structures differ from those of the defect-free surface over $\sim$ 1.3 nm (not shown here).

The observations above could explain the observed large drop in the M_{spin} values for the disordered samples. The atomic-defect sample contains $\sim$ 10 % of the disordered area within the surface. Assuming an isotropic electronic-structure modulation expanding from the defect, most of the Fe atoms at the surface could electronically differ from those of the defect-free Fe_2N. If the M_{spin} value distributed from nearly zero at the defect center to an ideal one for the Fe_2N far enough from the defect, the atomic-defect sample could have the observed M_{spin} value on average. The less-ordered sample, whose surface is mostly composed of the disordered structures, would suffer a further decrease in the magnetic moment. Therefore, the coexistence of such magnetically-weak Fe atoms near the defect could explain the non-linear dependence of the M_{spin} values on the R_{order}. This gives an important conclusion that the perfect lattice ordering in an atomic scale, beyond the resolution of macroscopic structural characterizations, is indispensable to obtain monolayer Fe_2N with an ideal magnetic moment.

5.4 Conclusion

We have conducted a detailed study on the impact of the atomic defects on the surface electronic structures of the monolayer Fe_2N on Cu(001). The degree of the surface lattice ordering showed large dependence on the annealing temperature, and the weakly-annealed samples contained a fraction of the structural disorder. The amount of the disorder could not account for the sudden drop of the M_{spin} value, especially observed in the atomic-defect sample. The atomically-resolved STS measurements could reveal the modulation of the surface electronic structures in a large area around the defect, which possibly explains the observed deterioration of the sample ferromagnetism. The present work establishes the importance of a microscopic structural characterization to discuss 2D ferromagnetism, which stems from ideal atomic/spin structures and thus can be easily modulated by structural perturbation even in an atomic scale.

Chapter 6

Thickness-dependent electronic and magnetic properties of γ'-Fe_4N multilayers on Cu(001)

6.1 Introduction

Iron nitrides, especially in iron-rich phases, have been under intense research due to the strong ferromagnetism and interest in its physical origin [37, 101]. The difficulty in obtaining a single phase has been a long-standing problem for ferromagnetic iron nitrides, to hinder fundamental understanding of intrinsic physical properties [102–104]. Recently, the successful epitaxial growth of single-phase ferromagnetic γ'-Fe_4N has been reported on various substrates, which helps to comprehend a crucial role for the hybridization between Fe and N states in the ferromagnetism of γ'-Fe_4N [43, 44, 105–109]. The robust Fe-N bonding also renders an Fe_2N layer strongly two-dimensional [19], which possibly facilitates a layer-by-layer stacking of γ'-Fe_4N on metals. This contrasts with the case of elemental $3d$ transition metals (TMs) deposited on $3d$ TM substrates, in which inevitable atom intermixing and exchange of constituents prevent the formation of ordered overlayers [110–112]. Therefore, the investigation into the electronic and magnetic states of γ'-Fe_4N atomic layers can not only elucidate the layer-/site-selective electronic and magnetic states of γ'-Fe_4N, but unravel the origin of the strongly thickness-dependent physical properties in a thin-film limit of $3d$ TM ferromagnets [29–36].

Here, we report two growth modes of γ'-Fe_4N/Cu(001) depending on preparation methods. The scanning tunneling microscopy/spectroscopy (STM/STS) observations indicated a successful growth of ordered trilayer γ'-Fe_4N, without extra nitrogen bombardment onto the existing structures. X-ray absorption spectroscopy/magnetic circular dichroism (XAS/XMCD) measurements revealed the thickness dependence of the magnetic moments of Fe atoms, the origin of which

was well explained by the first-principles calculations. Based on an atomically-resolved structural characterization of the system, the layer-by-layer electronic and magnetic states of the γ'-Fe_4N atomic layers have been understood from both experimental and theoretical points of view.

6.2 Experiment

A clean Cu(001) surface was prepared by repetition of sputtering with Ar^+ ions and subsequent annealing at 820 K. Iron was deposited at room temperature (RT) in a preparation chamber under an ultrahigh vacuum (UHV) condition ($< 1.0 \times 10^{-10}$ Torr), using an electron-bombardment-type evaporator (EFM, FOCUS) from a high-purity Fe rod (99.998 %). The STM measurements were performed at 77 K in UHV ($< 3.0 \times 10^{-11}$ Torr) using electrochemically etched W tips. The differential conductance $\mathrm{d}I/\mathrm{d}V$ was recorded for STS using a lock-in technique with a bias-voltage modulation of 20 mV and 719 Hz. The XAS and XMCD measurements were performed at BL 4B of UVSOR-Ⅲ [59, 61] in a total electron yield (TEY) mode. The degree of circular polarization was ~ 65 %, and the x-ray propagation vector lay within the $(1\bar{1}0)$ plane of a Cu(001) substrate. All the XAS/XMCD spectra were recorded at ~ 8 K, with external magnetic field B up to ± 5 T applied parallel to the incident x-ray. The symmetry and quality of the surface were also checked by low energy electron diffraction (LEED) in each preparation chamber. First-principles calculations were performed within the density functional theory in the local density approximation [113], using a self-consistent full-potential Green function method specially designed for surfaces and interfaces [114, 115].

6.3 Results and Discussion

6.3.1 Monolayer and bilayer-dot γ'-Fe_4N

Monolayer Fe_2N on Cu(001) was prepared prior to any growth of multilayer γ'-Fe_4N by the following cycle: N^+ ion bombardment with an energy of 0.5 keV to a clean Cu(001) surface, subsequent Fe deposition at RT, and annealing at 600 K. Note that the monolayer Fe_2N is identical to Fe_4N on Cu(001) in a monolayer limit, and thus referred to as also "monolayer γ'-Fe_4N" hereafter. A topographic image of the sample after one growth cycle is shown in Fig. 6.1(a). The monolayer γ'-Fe_4N is formed on the Cu terraces at ~ 0.85 ML coverage. An atomically-resolved image of that surface displayed in Fig. 6.1(b) reveals a clear dimerization of the Fe atoms,

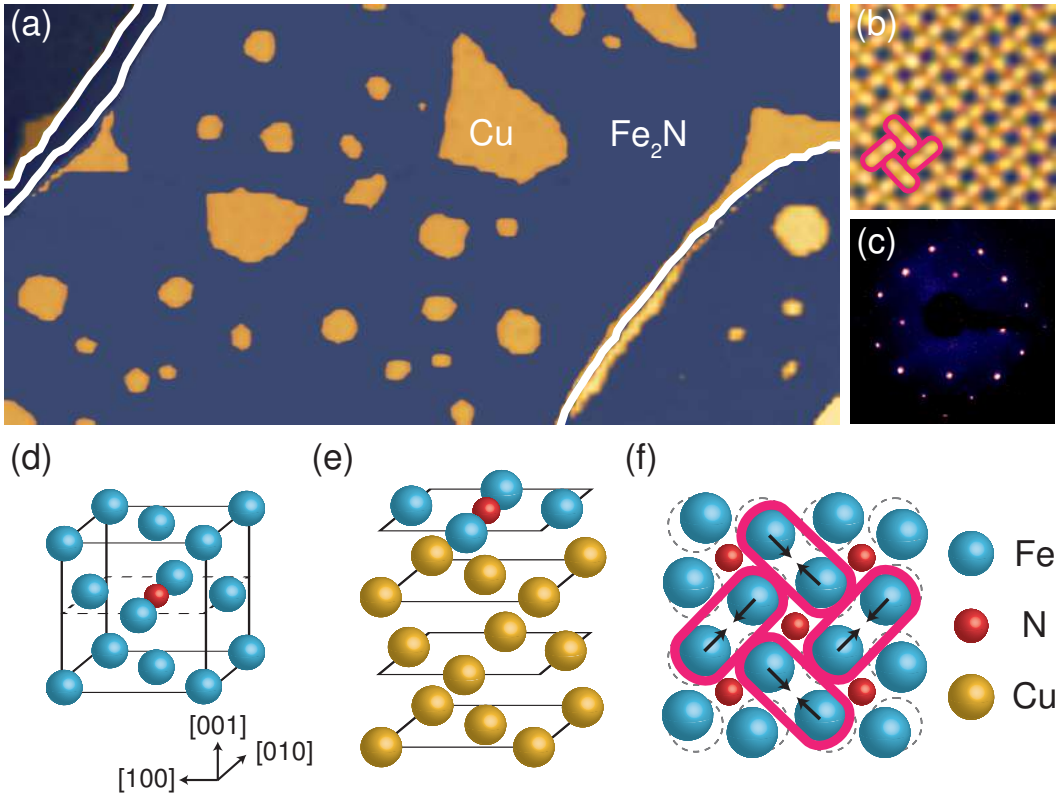

Figure 6.1: (Color online) Topography and atomic structure of the monolayer γ'-Fe_4N on Cu(001). (a) Topographic image (100×50 nm^2, sample bias $V_s = +1.0$ V, tunneling current $I = 0.1$ nA) of the monolayer γ'-Fe_4N on Cu(001). White lines represent step edges of the Cu(001) terraces. Color contrast is enhanced within each terrace. (b) Close view (2.5×2.5 nm^2, $V_s = 0.25$ V, $I = 45$ nA) of the surface Fe_2N layer. The dimerization of Fe atoms is indicated by encirclement. (c) LEED pattern obtained with an incident electron energy of 100 eV. (d) Bulk crystal structure of γ'-Fe_4N. A dotted parallelogram represents an Fe_2N plane. (e) Atomic structure of the monolayer γ'-Fe_4N on Cu(001). (f) Schema illustrating $p4g(2 \times 2)$ reconstruction in the surface Fe_2N layer of γ'-Fe_4N. Arrows indicate the shift of the Fe atoms from an unreconstructed $c(2 \times 2)$ coordination (dotted circles). For (d) to (f), large blue (yellow) and small red spheres represent Fe (Cu) and N atoms, respectively.

typical of ordered γ'-Fe_4N on Cu(001) [38, 97]. A LEED pattern of the surface is shown in Fig. 6.1(c), which exhibits sharp spots with the corresponding $p4g(2 \times 2)$ symmetry. It is known that [38–40, 97] the topmost layer of the γ'-Fe_4N on Cu(001) always consists of the Fe_2N plane in a bulk Fe_4N crystal shown in Fig. 6.1(d). A schematic model of the monolayer γ'-Fe_4N is given in Fig. 6.1(e), composed of a single Fe_2N plane on Cu(001). Accordingly, the surface Fe_2N plane takes reconstruction to the $p4g(2 \times 2)$ coordination [38], in which the Fe atoms dimerize in two perpendicular directions as illustrated in Fig. 6.1(f).

After repeating the growth cycles, we found a new structure different from the monolayer γ'-Fe_4N. Figure 6.2(a) displays the surface after two growth cycles in total, namely, another cycle of the N^+ ion bombardment, Fe deposition, and annealing onto the existing monolayer γ'-Fe_4N surface. Then, the surface becomes mostly covered with the monolayer γ'-Fe_4N, which contains a small number of bright dots. For a structural identification of these dots, we measured atomically-resolved topographic images and line profiles at different V_s as shown in Fig. 6.2(b) and 6.2(c). The dot structure imaged at $V_s = -0.1\ V$ reveals the dimerization of the Fe atoms as the monolayer γ'-Fe_4N surface. This indicates that the topmost part of the dot consists of the reconstructed Fe_2N. At positive V_s of +0.1 V, in contrast, the dot is recognized as a single protrusion both in the topographic image and line profile, while the surrounding monolayer γ'-Fe_4N still shows the Fe dimerization. This implies the different electronic structure of the dot compared to the monolayer γ'-Fe_4N, which comes from the difference in a subsurface atomic structure.

The observed height difference between the dot and the monolayer γ'-Fe_4N ranges from 4 to 10 pm depending on V_s. These values are in the same order of a lattice mismatch between the bulk crystals of the γ'-Fe_4N/Cu(001) (380 pm) and Cu(001) (362 pm) [38], but an order of magnitude smaller than the lattice constant of the γ'-Fe_4N/Cu(001). This suggests that the topmost layer of the dot is not located above the monolayer γ'-Fe_4N surface, but shares the Fe_2N plane with. Furthermore, the bright dot is composed of only four pairs of the Fe dimer as imaged in Fig. 6.2(b), indicating that the difference in the atomic and/or electronic structures is restricted within a small area. Considering the above, it is most plausible that one Fe atom is embedded just under the surface N atom at the dot center, and thus a bilayer γ'-Fe_4N dot is formed as schematically shown in Fig. 6.2(d). This structure corresponds to a minimum unit of the bilayer γ'-Fe_4N on Cu(001).

This bilayer dot formed clusters by a further repetition of the growth cycles. Figure 6.3(a) shows an enlarged view of the iron-nitride surface after two growth cycles. The coverage of the dot is estimated to be ~ 5 % of the entire surface. Another growth cycle onto this surface led to an increase in a dot density up to ~ 40 %, as shown in Fig. 6.3(b). However, further repetitions of the cycles resulted in neither a considerable increase in the dot density nor the formation of a continuous

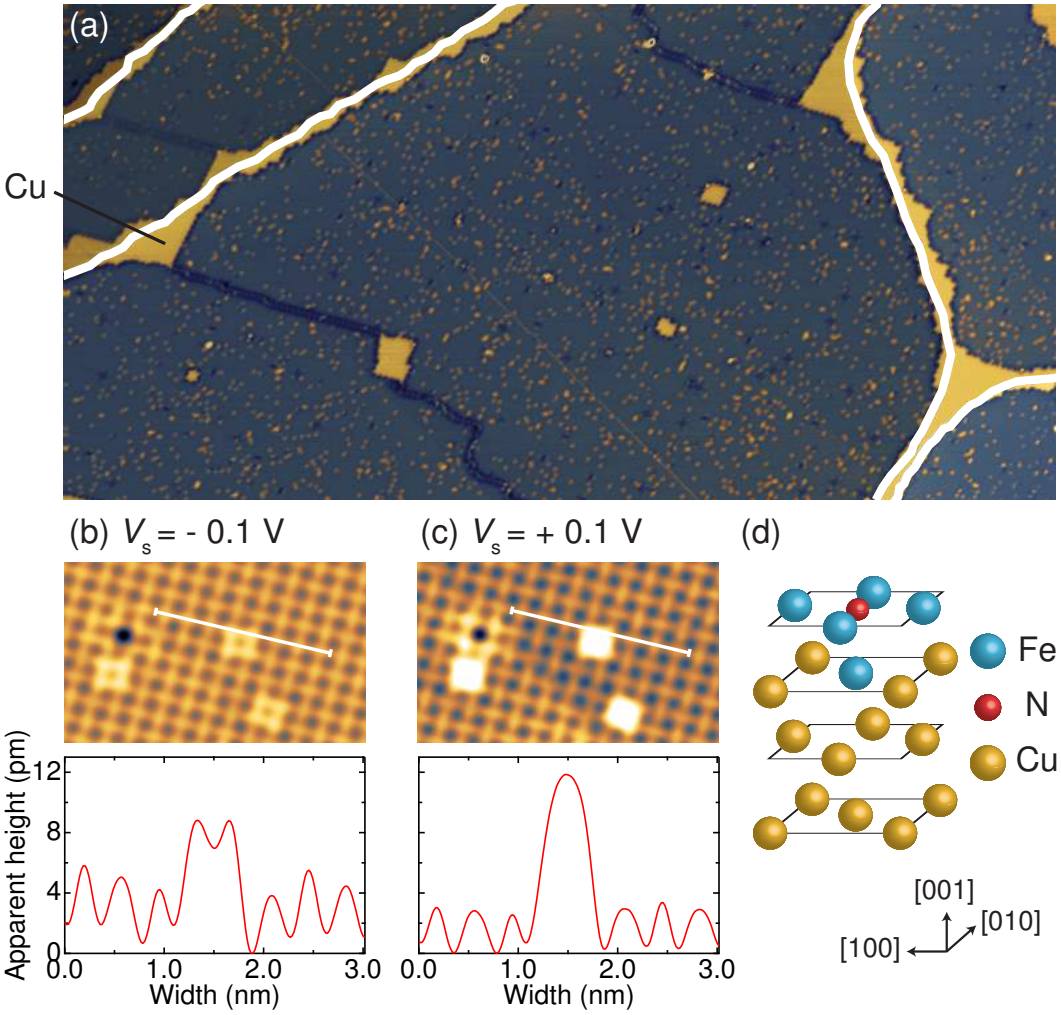

Figure 6.2: (Color online) Topography of the bilayer γ'-Fe_4N dot on Cu(001). (a) Topographic image (120×60 nm^2, $V_s = -0.1$ V, $I = 0.1$ nA) of the monolayer (darker area) and dot-like bilayer γ'-Fe_4N on Cu(001). White lines represent step edges of the Cu(001) terraces. Color contrast is enhanced within each terrace. (b,c) Upper panels: Atomically-resolved topographic images (7×3 nm^2, $I = 2.0$ nA) taken at (b) $V_s = -0.1$ V and (c) $+0.1$ V. Lower panels: Height profiles measured along lines indicated in the upper panels. (d) Proposed atomic structure of the bilayer-dot γ'-Fe_4N on Cu(001). Large blue (yellow) and small red spheres correspond to Fe (Cu) and N atoms, respectively.

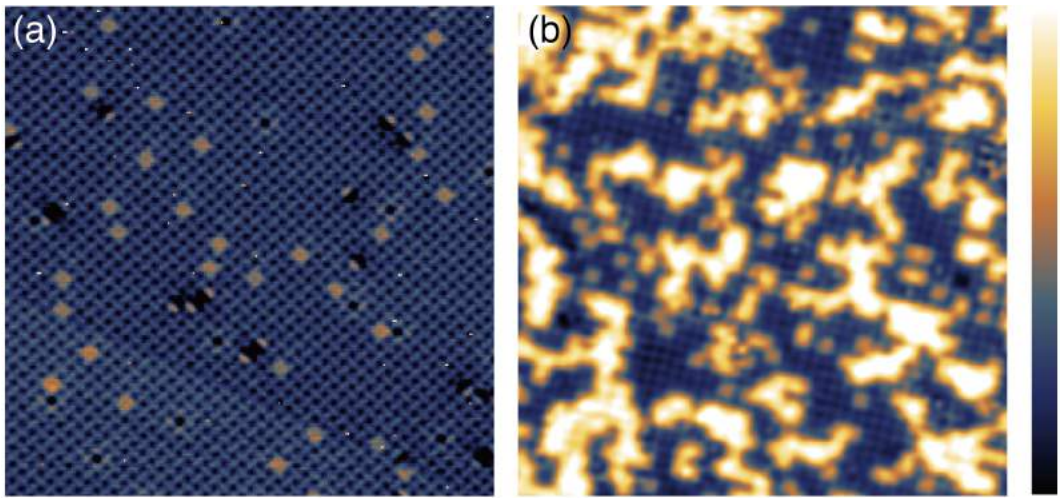

Figure 6.3: (Color online) Topographic images (15×15 nm^2) of the surface after repetition of (a) two and (b) three growth cycles. The set point is (V_s, I) = (+0.25 V, 5.0 nA) for (a) and (+0.1 V, 3.0 nA) for (b).

bilayer film. This can be attributed to an inevitable sputtering effect in every growth cycle: an additional N^+ ion bombardment to the existing surface not only implanted N^+ ions but also sputtered the surface, which caused the loss of the iron nitrides already formed at the surface, as well as the increase in the surface roughness.

To compensate this loss of surface Fe atoms by the sputtering effect, we also tried to increase the amount of deposited Fe per cycle. Nonetheless, the number of Fe atoms, which remained at the surface after annealing, did not increase possibly because of the thermal metastability of Fe/Cu systems [116–119]. The isolated Fe atoms without any bonding to N atoms were easily diffused and embedded into the Cu substrate during the annealing process. As a result, only the imperfect bilayer γ'-Fe_4N was obtained through this method.

6.3.2 Trilayer γ'-Fe_4N film

Multilayer γ'-Fe_4N films were obtained by the following procedure. First, the monolayer γ'-Fe_4N was prepared on Cu(001) as above. Then, 2 ML Fe was deposited under N_2 atmosphere (5.0×10^{-8} Torr)[1] at RT, and the sample was annealed

[1] We checked the ionization of nitrogen molecules/atoms without bombardment using an ion gun. The ion flux monitored for the Fe evaporator increased in proportion to the rise in the N_2 pressure, far below the parameters at which Fe started to be evaporated. This indicates the ionization of the N_2 molecules and/or N atoms around the evaporator possibly by thermal electrons created inside it. Then, the N^+ and N_2^+ ions could reach to the surface together with the evaporated Fe atoms, or iron nitride was already formed before landing.

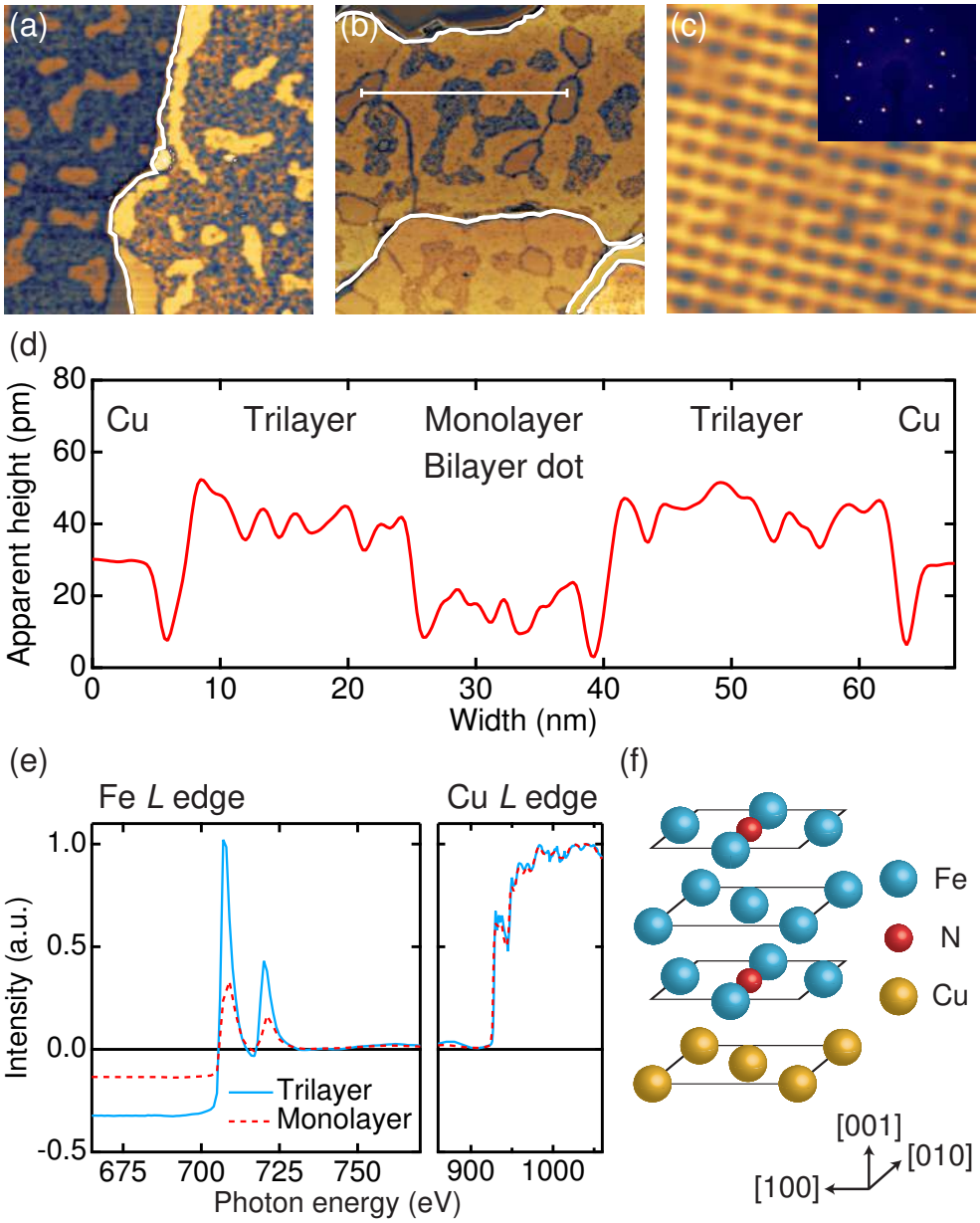

Figure 6.4: (Color online) Topography of the trilayer γ'-Fe_4N film on Cu(001). Topographic images (100×100 nm^2) after (a) two and (b) three cycles of the Fe deposition under N_2 atmosphere and subsequent annealing onto the monolayer γ'-Fe_4N on Cu(001). The setpoint is $I = 0.1$ nA, $V_s = -0.1$ V for (a) and -0.05 V for (b). White lines indicate step edges of the Cu terraces. Color contrast is enhanced within each terrace. (c) Atomically-resolved topographic image (4×4 nm^2, $I = 5.0$ nA, $V_s = -0.1$ V) of the trilayer γ'-Fe_4N surface. An inset represents a LEED pattern of the sample shown in (b), obtained with an incident electron energy of 100 eV. (d) Height profile measured along the line indicated in (b). (e) XAS edge jump spectra of the trilayer (solid) and monolayer (dotted) samples at the Fe and Cu L edges. The intensity is normalized to the Cu edge jump. (f) Atomic model expected for the trilayer γ'-Fe_4N on Cu(001). Blue (yellow) large and red small spheres represent Fe (Cu) and N atoms, respectively.

at 600 K. Figures 6.4(a) and 6.4(b) show topographic images after two and three above mentioned cycles, respectively. In the images, the coverage of new bright area, different from the imperfect bilayer dot, monotonously increases with repeating the cycles. A close view of that new surface is displayed in Fig. 6.4(c), revealing the dimerized (or even $c(2 \times 2)$-like dot) structures. Because a LEED pattern shown in the inset of Fig. 6.4(c) exhibits the $p4g(2 \times 2)$ symmetry without extra spots, the topmost layer of this surface is composed of the reconstructed Fe_2N plane [97]. Therefore, these observations suggest that the new area would consist of γ'-Fe_4N other than both of the monolayer and bilayer dot.

In order to determine the structure of this newly obtained γ'-Fe_4N, a typical height profile of the surface was recorded as shown in Fig. 6.4(d). It is clear that the new structure is higher than both the Cu surface and the surface including the monolayer/dot-like bilayer γ'-Fe_4N. This suggests that the new area is composed of γ'-Fe_4N thicker than bilayer. Quantitative information on the thickness of the new structure could be obtained from Fe L $(2p \rightarrow 3d)$ edge jump spectra shown in Fig. 6.4(e), whose intensity is roughly proportional to the amount of surface/subsurface Fe atoms. The sample prepared in the same procedure as that shown in Fig. 6.4(b) reveals an edge jump value of 0.32, while the monolayer γ'-Fe_4N 0.12[2]. Considering that the new area occupies $\sim$ 60 % of the entire surface as deduced from Fig. 6.4(b), the thickness of this γ'-Fe_4N must be less than quadlayer to meet the experimental edge jump value of 0.32 (See Appendix C). Hence, the newly obtained structure is identified as a trilayer γ'-Fe_4N film. An atomic structure expected for the trilayer γ'-Fe_4N on Cu(001) is presented in Fig. 6.4(f). The growth without any ion bombardment to the monolayer surface possibly stabilizes the subsurface pure Fe layer, which could promote the formation of the trilayer γ'-Fe_4N film in a large area.

Finally, let us mention another growth method of the γ'-Fe_4N film. We previously report a possible layer-by-layer growth of the γ'-Fe_4N atomic layers on Cu(001), by the N^+ ion bombardment with a relatively low energy of 0.15 kV [45]. This soft implantation of N^+ ions successfully avoids extra damage to the existing γ'-Fe_4N structures during the repetition of the growth cycles. The reported different electronic/magnetic states could then originate from the difference in the fabrication processes. Another finding is that, in the current study, only the monolayer and trilayer γ'-Fe_4N could be obtained in a continuous film form. This implies that an Fe_2N-layer termination would be preferable through the present methods, possibly due to the metastability of an interface between Cu and pure Fe layers [116–119].

[2]The amount of the Fe atoms detected in the edge-jump spectra was smaller than that expected from the initially deposited ones. This implies that a certain amount of Fe atoms, not participating in forming any γ'-Fe_4N structures, was embedded into the Cu substrate during annealing, at least several nms (probing depth in the TEY mode) below the surface.

6.3.3 Electronic and magnetic properties of γ'-Fe_4N atomic layers

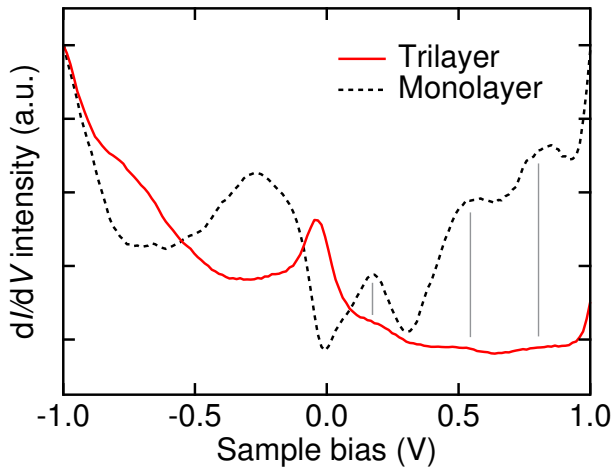

Figure 6.5: (Color online) Surface electronic structures of the γ'-Fe_4N on Cu(001). Experimental dI/dV spectra recorded above the trilayer (solid) and monolayer (dotted) γ'-Fe_4N surfaces are presented. The dI/dV intensity is arbitrary. A STM tip was stabilized at $V_s = +1.0$ V, $I = 3.0$ and 7.0 nA for the trilayer and monolayer surfaces, respectively. Gray lines are guide to the eye.

The surface electronic structures of γ'-Fe_4N showed large dependence on the sample thickness. Figure 6.5 displays experimental dI/dV spectra measured on the surfaces of the trilayer and monolayer γ'-Fe_4N. The peaks located at $V_s \sim$ +0.20, +0.55, and +0.80 V, mainly originating from the unoccupied states in the down-spin band characteristic of Fe local density of states (LDOS), are observed for both the trilayer and monolayer surfaces. A significant difference between the spectra is a dominant peak located around $V_s = -50$ mV observed only for the trilayer surface. This peak possibly originates from the LDOS peak located around $E - E_F = -0.2$ eV, calculated for the Fe atoms not bonded to N atoms in the subsurface Fe layer [corresponding site of Fe4 shown in Fig. 6.7(b)]. Because of the $d_{3z^2-r^2}$ orbital character, this peak could be dominantly detected in the STS spectrum for the trilayer surface. Thus, the appearance of this additional peak could support the different subsurface structure of the trilayer sample, especially, the existence of the subsurface Fe layer proposed above.

The entire electronic and magnetic properties of the sample, including both surface and subsurface information, were investigated by using XAS and XMCD

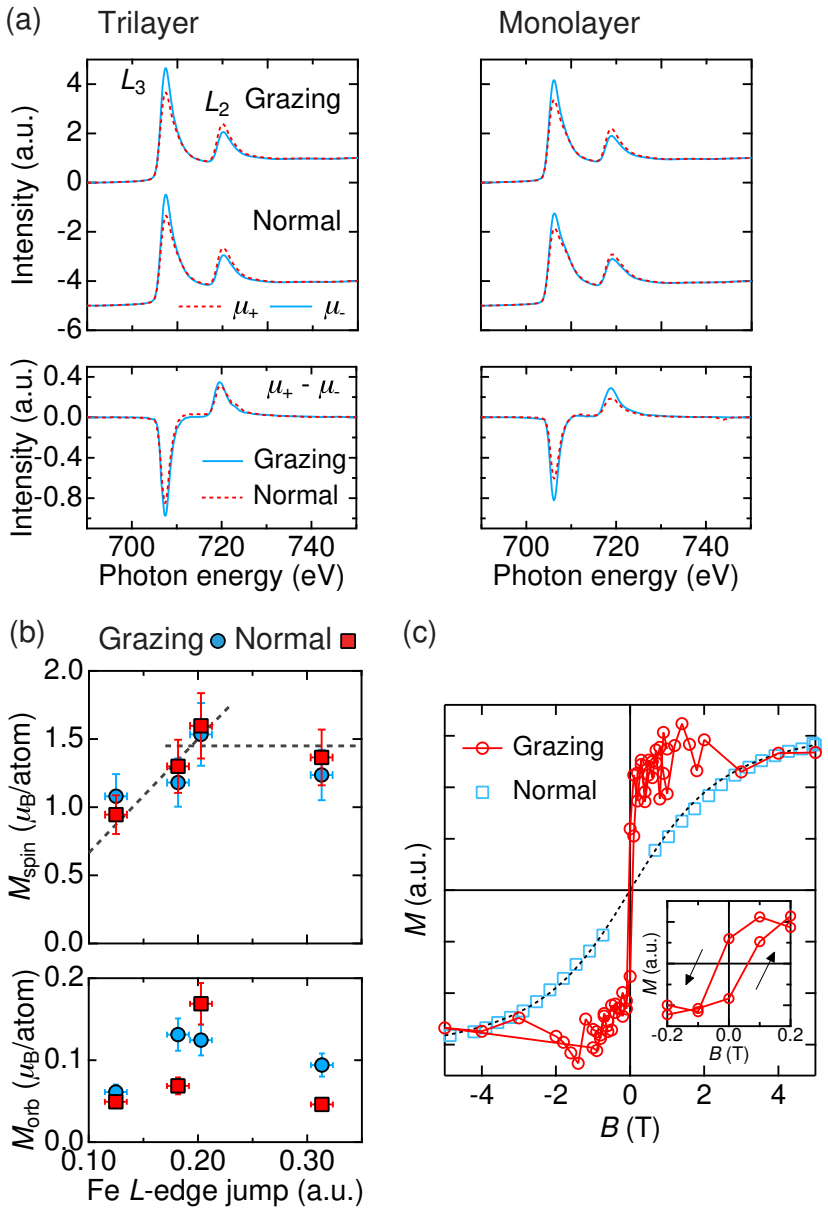

Figure 6.6: (Color online) Thickness-dependent electronic and magnetic properties of the γ'-Fe$_4$N atomic layers on Cu(001). (a) Upper panels: XAS spectra under $B = \pm 5$ T of the trilayer (left) and monolayer (right) samples in the grazing (top) and normal (bottom) incidence. Lower panels: Corresponding XMCD spectra in the grazing (solid) and normal (dotted) incidence. All the spectra are normalized to the Fe XAS L-edge jump. (b) Upper [lower] panel: Experimental spin [orbital] magnetic moment in the grazing (circle) and normal (square) incidence plotted with respect to the Fe L-edge jump values. The edge jump values of 0.12 and 0.32 correspond to those of the monolayer and trilayer samples, respectively. Dotted lines are guide to the eye. Error bars are indicated to all the data, and smaller than the marker size if not seen. (c) Magnetization of the monolayer sample recorded in the grazing (circle and line) and normal (square) incidence. A dotted line is the guide to the eye. An inset shows an enlarged view of the curve recorded in the grazing incidence.

techniques at the Fe $L_{2,3}$ ($2p_{1/2,3/2} \rightarrow 3d$) absorption edges. Figure 6.6(a) shows XAS ($\mu_+,\ \mu_-$) and XMCD ($\mu_+ - \mu_-$) spectra under $B = \pm 5\ T$ of the trilayer and monolayer samples in the grazing ($\theta = 55°$) and normal incidence ($\theta = 0°$). Here, μ_+ (μ_-) denotes a x-ray absorption spectrum with the photon helicity parallel (antiparallel) to the Fe $3d$ majority spin, and an incident angle θ is defined as that between the sample normal and incident x-ray. The trilayer (monolayer) sample was prepared in the same procedure as that shown in Fig. 6.4(b) [Fig. 6.1(a)]. It is clear that the XMCD intensity is larger in the trilayer one, indicating an enhancement of magnetic moments with increasing thickness.

For a further quantitative analysis on the magnetic moments, we applied XMCD sum rules [49, 50] to the obtained spectra and estimated spin ($M_{\rm spin}$) and orbital ($M_{\rm orb}$) magnetic moments separately. Note that the average number of $3d$ holes ($n_{\rm hole}$) of 3.2 was used in the sum-rule analysis, which was estimated by comparing the area of the experimental XAS spectra with that of a reference spectrum of bcc Fe/Cu(001) ($n_{\rm hole} = 3.4$) [47]. The thickness dependence of the $M_{\rm spin}$ and $M_{\rm orb}$ values is summarized in Fig. 6.6(b). The value of $M_{\rm spin}$ increases monotonously with increasing the Fe L-edge jump value, namely, an average sample thickness, and finally saturates at $\sim 1.4\ \mu_{\rm B}$/atom in the trilayer sample (corresponding edge jump value of 0.32). The change in $M_{\rm orb}$ is not so systematic relative to $M_{\rm spin}$, however, the $M_{\rm orb}$ values seem to be enhanced in the grazing incidence. This implies an in-plane easy magnetization of the γ'-Fe_4N atomic layers on Cu(001), also consistent with the previous reports on the γ'-Fe_4N thin films on Cu(001) [44, 45]. Figure 6.6(c) shows magnetization curves of the monolayer sample, whose intensity corresponds to the L_3-peak XAS intensity normalized to the L_2 one. The curve recorded in the normal incidence shows negligible remanent magnetization. On the other hand, that in the grazing one draws a rectangular hysteresis loop, which confirms the in-plane easy magnetization. The coercivity of the monolayer sample is estimated to be $\sim$ 0.05 T at 8.0 K, larger than $\sim$ 0.01 T for 5 ML Fe/Cu(001) [33], $\sim$ 1 mT for 5 ML Fe/GaAs(100)-(4×6) [120] and the 30 nm thick γ'-Fe_4N film [44] at RT.

6.3.4 Theoretical analysis on the electronic and magnetic states of γ'-Fe_4N atomic layers on Cu(001)

The observed thickness dependence of the magnetic moments can be well understood with a help of first-principles calculations. Figures 6.7(a) and 6.7(b) show layer-resolved DOS of the monolayer and trilayer γ'-Fe_4N on Cu(001), respectively. Here, non-equivalent Fe sites in each layer are distinguished by different numbering. In particular, the Fe atoms at the Fe3 (Fe4) site in the trilayer γ'-Fe_4N

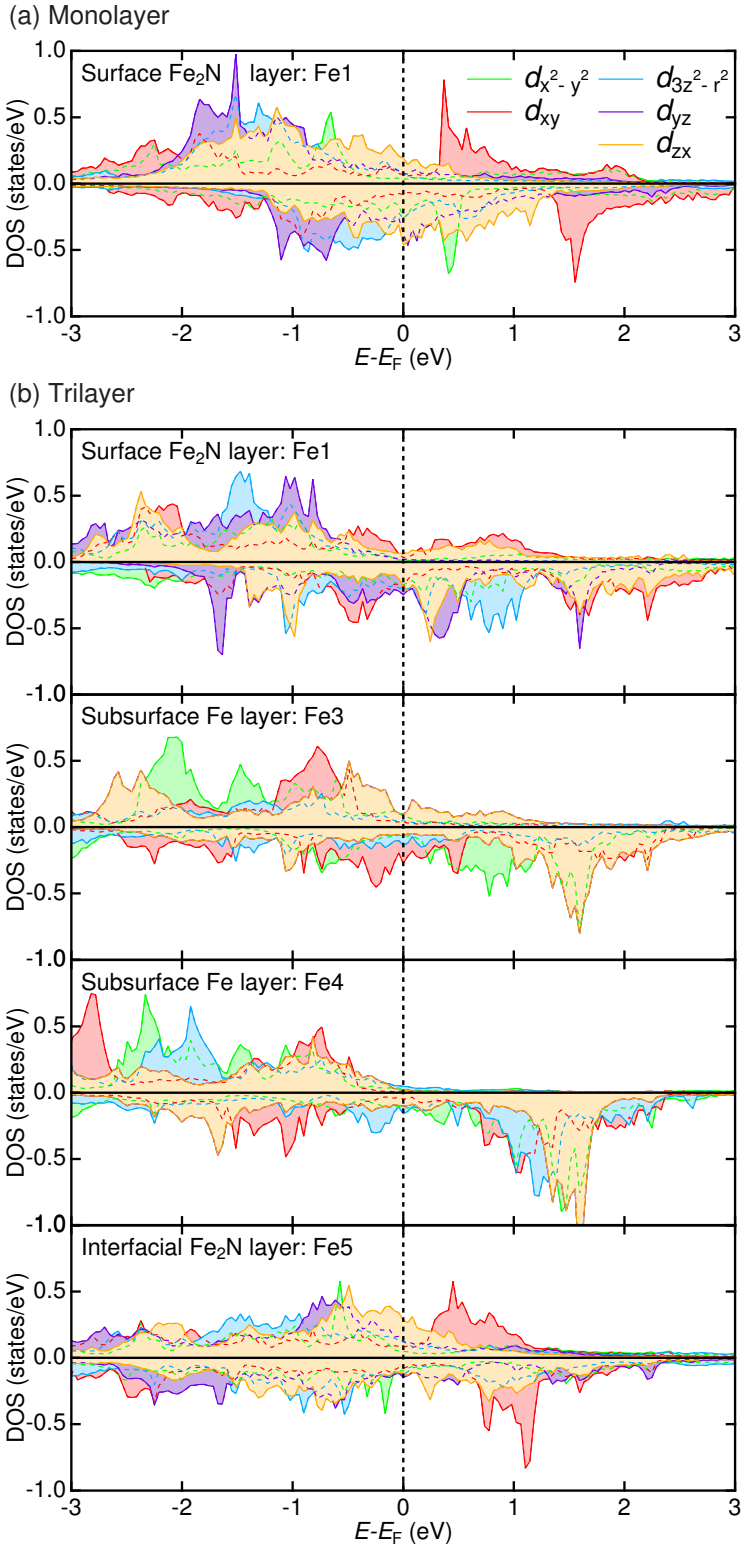

Figure 6.7: (Color online) Layer-by-layer electronic states of the γ'-Fe_4N atomic layers on Cu(001). Calculated layer-resolved DOS projected to each $3d$ orbital of the (a) monolayer and (b) trilayer γ'-Fe_4N on Cu(001). The DOS in the up-(down-) spin band is shown at upper (lower) panels. Note that the states with d_{yz} and d_{zx} orbitals are degenerated for the Fe3 and Fe4 sites in (b).

Table 6.1: Calculated atomic magnetic moments of the Fe atoms at each site (in units of μ_{B}/atom). The site notation is the same as that used in Fig. 6.7.

	Surface Fe_2N		Subsurface Fe		Interfacial Fe_2N	
	Fe1	Fe2	Fe3	Fe4	Fe5	Fe6
Monolayer	1.1	1.1	-	-	-	-
Trilayer	1.8	1.8	2.0	3.0	0.62	0.62

correspond to those with (without) a bond to N atoms[3]. In Table 6.1, calculated values of an atomic magnetic moment M_{atom}, corresponding to M_{spin} + M_{orb} along the easy magnetization direction, are also listed. In the monolayer case, the calculated M_{atom} is 1.1 μ_{B}/atom, which is in perfect agreement with the experimental value. This supports an ideal atomic structure of our monolayer sample.

Interestingly, the value of M_{atom} for the Fe atoms in the monolayer γ'-Fe_4N is more than 1.5 times smaller than that in the topmost layer of the trilayer one (1.83 μ_{B}/atom). In comparison with the DOS shown at the top of Fig. 6.7(b), the impact of the hybridization with the Cu states on the Fe DOS can be seen in Fig. 6.7(a): First, the DOS in the up-spin band, especially with $d_{3\mathrm{z}^2-\mathrm{r}^2}$ and d_{yz} orbitals, becomes to have a tail toward a higher-energy side across the E_{F}. This change deviates the $3d$ electrons in the up-spin band from a fully-occupied nature. Moreover, the spin asymmetry of the occupied $3d$ electrons, the difference between the electron occupation into each spin band normalized by the sum of them, reduces especially for the DOS with d_{xy}, $d_{3\mathrm{z}^2-\mathrm{r}^2}$ and d_{yz} orbitals. These changes could decrease M_{spin} of the Fe atoms. Note that the similar reduction in the magnetic moments of $3d$ TMs due to the hybridization with Cu states is reported, for example, in Ref. 121, 122.

Then, by comparing two different Fe_2N interfaces with the Cu substrate, it turns out that M_{atom} of the monolayer γ'-Fe_4N (1.1 μ_{B}/atom) is almost twice compared to that of the trilayer one (0.62 μ_{B}/atom). In the monolayer case, the Fe_2N layer faces to a vacuum and the Fe atoms are under reduced atomic coordination. This results in the narrower band width, and thus the DOS intensity increases in the vicinity of E_{F}. Accordingly, a larger exchange splitting can be possible and the spin asymmetry of the occupied $3d$ electrons increases as shown in Fig. 6.7(a), compared to the interfacial Fe_2N layer of the trilayer γ'-Fe_4N [bottom panel of Fig. 6.7(b)]. This leads to larger magnetic moments at the surface. As a result, the competition between the enhancement at the surface and the decrease at the interface would make M_{atom} values quite layer-sensitive.

In the subsurface Fe layer of the trilayer γ'-Fe_4N, the value of M_{atom} becomes largest due to the bulk coordination of the Fe atoms. Especially the Fe atoms not

[3]The difference of DOS between (Fe1, Fe2) in the monolayer γ'-Fe_4N, (Fe1, Fe2) and (Fe5, Fe6) in the trilayer one is just a switch of the orbital assignment between d_{yz} and d_{zx}. Therefore, the DOS of Fe2 in the monolayer γ'-Fe_4N, Fe2 and Fe6 in the trilayer one is not presented here.

bonded to the N ones possess M_{atom} of 3.0 μ_{B}/atom, which is comparable to the values of Fe atoms at the same site in the bulk γ'-Fe_4N [37]. Consequently, by averaging the layer-by-layer M_{atom} values of the trilayer γ'-Fe_4N, the total magnetic moment detected in the XMCD measurement is expected to be 1.7 μ_{B}/Fe, with the electron escape depth taken into account (See Appendix C). Considering the composition expected to the trilayer sample, this value can well explain the experimental one of $\sim$ 1.5 μ_{B}/Fe.

The theory also demonstrates the direction of an easy magnetization axis. The in-plane easy magnetization of our γ'-Fe_4N samples was confirmed by the magnetization curves as well as the incidence dependence of the M_{orb} value. In contrast, the pristine ultrathin Fe films, which form either fct or fcc structures on Cu(001), show uncompensated out-of-plane spins over a few surface layers [36, 123]. This shift of magnetic anisotropy by nitridation can be understood from the orbital-resolved Fe DOS shown in Figs. 6.7(a) and 6.7(b). Unlike the pure Fe/Cu(001) system [124], the occupation of $3d$ electrons in states with out-of-plane-oriented orbitals ($d_{\mathrm{yz}},\ d_{\mathrm{zx}},\ d_{3\mathrm{z}^2-\mathrm{r}^2}$) is considerably larger than that with in-plane-oriented ones ($d_{\mathrm{xy}},\ d_{\mathrm{x}^2-\mathrm{y}^2}$). This could make M_{orb} prefer to align within a film plane, resulting in the in-plane magnetization of the system [125].

6.4 Conclusion

In conclusion, we have conducted a detailed study on the growth, electronic and magnetic properties of the γ'-Fe_4N atomic layers on Cu(001). The ordered trilayer film of γ'-Fe_4N can be prepared by the Fe deposition under N_2 atmosphere onto the existing monolayer surface. On the other hand, the repetition of the growth cycles including the high-energy N^+ ion implantation resulted in the imperfect bilayer γ'-Fe_4N. The STM and STS observations revealed the change in the surface topography and electronic structures with increasing the sample thickness. The XAS and XMCD measurements also showed the thickness dependence of the spectra, and the corresponding evolution of the M_{spin} values. All the thickness dependence of the electronic and magnetic properties is well explained by the layer-resolved DOS calculated using the first principles. Structural perfection of the system makes it possible to fully comprehend the layer-by-layer electronic/magnetic states of the γ'-Fe_4N atomic layers.

Appendix

A Simulation of simple broadening for surface wave functions

In the STM observation, two adjacent objects imaged at short tip-surface distance usually appear to be broader structures when the tip is sufficiently far from the surface. This is due to simple broadening of LDOS distribution, accompanied by the decay of the surface wave functions. Here, we check the possibility that the observed tunneling-current dependence of the line profiles can be explained by this kind of simple broadening. As a first approximation, we use a summation of Gaussian functions $f_{\rm G}$ to reproduce six peaks observed in the line profiles at higher I. A numerical expression $f_{\rm profile}$ is given in the following form,

$$\begin{aligned} f_{\rm profile}\left(x, x_{\rm h}, \sigma_{\rm h}, x_{\rm l}, \sigma_{\rm l}\right) &= A_{\rm h}\{f_{\rm G}\left(x, x_{\rm h}, \sigma_{\rm h}\right) + f_{\rm G}\left(x, -x_{\rm h}, \sigma_{\rm h}\right) \\ &\quad + f_{\rm G}\left(x, 2x_{\rm l} - x_{\rm h}, \sigma_{\rm h}\right) + f_{\rm G}\left(x, -2x_{\rm l} + x_{\rm h}, \sigma_{\rm h}\right)\} \\ &\quad + A_{\rm l}\left\{f_{\rm G}\left(x, x_{\rm l}, \sigma_{\rm l}\right) + f_{\rm G}\left(x, -x_{\rm l}, \sigma_{\rm l}\right)\right\}, \qquad (6.1) \\ \text{where} \quad f_{\rm G}\left(x, x_0, \sigma\right) &= \frac{1}{\sqrt{2\pi\sigma^2}} \exp\left[-\frac{\left(x - x_0\right)^2}{2\sigma^2}\right], \end{aligned}$$

$x_{\rm h}$ $(x_{\rm l})$, $\sigma_{\rm h}$ $(\sigma_{\rm l})$ and $A_{\rm h}$ $(A_{\rm l})$ are a center position, standard deviation and normalization coefficient of the Gaussian functions corresponding to four higher- (two lower-) intensity peaks in the line profiles, respectively. First, to analyze the charge distribution without considerable decay, the experimental line profile at I = 45 nA is fitted to Eq. (6.1). Thus simulated profile (solid line) is shown in the top panel of Fig. 6.8(a), well reproducing the experimental one (open circles). Note that all the profiles in Fig. 6.8(a) are normalized to the peak intensity, and dashed (dot-dashed) curves correspond to the first four (last two) terms in Eq. (6.1). Parameters extracted from the fitting are summarized in Table 6.2. Hereafter, for considering the decay of the surface wave functions at longer distances, only $\sigma_{\rm h}$ and $\sigma_{\rm l}$ are increased to the same extent, with $x_{\rm h}$ and $x_{\rm l}$ fixed. In Fig. 6.8(a), one can see that sharp peaks, recognized in the top panel, gradually become blunt with a broadening of the Gaussian functions, and finally form almost one broad structure at the center,

Table 6.2: Results of the fitting for the experimental line profile at I = 45 nA.

x_{h} (Å)	σ_{h} (Å)	x_{l} (Å)	σ_{l} (Å)
1.0	0.60	3.4	0.41

as shown in the bottom. A series of broadened line profiles is shown in the left of Fig. 6.8(b), in comparison with the current dependence of the experimental ones (the same in the manuscript). It is obvious that an increase in the σ value renders the simulated profiles deviated from the experimental ones, in terms of the width of the peak structures and relative peak intensities. Note that these discrepancy cannot be compensated even if different decay speeds are assumed for the Gaussian functions with σ_{h} and those with σ_{l}. Therefore, the simple broadening of the surface wave functions can be ruled out from a possible reason for the observed image change.

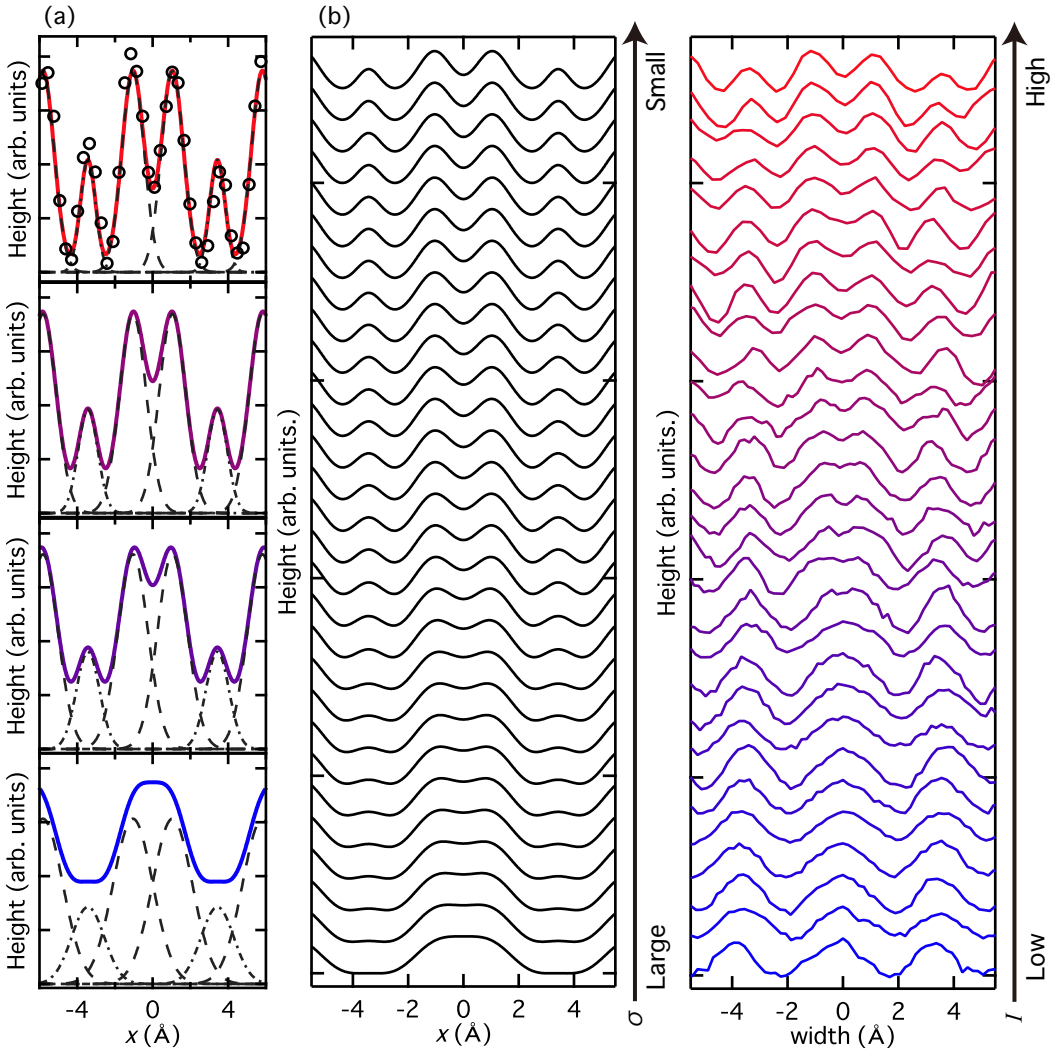

Figure 6.8: Demonstration of simple broadening of the charge density. (a) Simulated line profiles (solid) with $(\sigma_{\rm h},\ \sigma_{\rm l})$ = (0.60, 0.41), (0.70, 0.52), (0.80, 0.61), and (1.1, 0.90), from the top to the bottom, respectively. Each profile is decomposed into four (two) equal Gaussian functions indicated by dashed (dot-dashed) curves. Open circles in the top panel correspond to the experimental line profiles at I = 45 nA. (b) Simulated (experimental) line profiles are shown in the left (right). From the top to the bottom, σ (I) values become large (low).

B Estimated values of work function

Table 6.3: Values of work function Φ estimated for various pairs of I and V_{s}. Corresponding d values are also shown.

I (nA)	45	30	20	3.0	1.0	0.5	0.5	0.1
V_{s} (V)	0.25	0.4	0.5	0.2	0.2	0.25	0.5	0.25
d (Å)	2.6	2.9	3.2	3.6	4.0	4.4	4.8	5.1
Φ (eV)	5.52	5.42	5.43	5.61	5.57	5.52	5.41	5.56

All the measured I-z curves could be fitted to a single exponential function following Simmons' rule [77]. In Table 6.3, we summarize values of the work function Φ estimated from the fitting of several experimental I-z curves. No systematic change of the Φ value is observed depending on the combination of I and V_{s}, and also on d. As a result, a small variation in Φ allowed us to assume the constant Φ for the estimation of d.

C Conversion of XAS edge jump values to the thickness of γ'-Fe_4N

The escape probability of electrons from inside a sample to a vacuum depends on the depth at which the electrons are excited. For a numerical interpretation of the XAS edge jump, the following factors should be mainly considered in principle: the penetration length of an incident x-ray (λ_x) and electron escape depth (λ_e), both energy-dependent. In the case of a few atomic layers of $3d$ transition metals, the attenuation of the incident x-ray intensity is almost negligible because λ_x is orders of magnitude longer than the sample thickness [99]. Therefore, in the present case, only the electron escape probability at the depth z from the surface, namely, a factor of $\exp(-z/\lambda_e)$ is taken into account. As for the λ_e value of Fe, 17 Å was tentatively assumed in our analysis, which is experimentally determined for Fe thin films [99]. Then, based on the experimental Fe (N) edge jump values of 0.12 (0.015), those for the full-coverage dot-like bilayer, trilayer, and quadlayer γ'-Fe_4N on Cu(001) are calculated as summarized in Table 6.4.

Table 6.4: Experimental and calculated Fe (N) edge jump values for the monolayer, dot-like bilayer, trilayer, and quadlayer γ'-Fe_4N on Cu(001). In the calculation, each γ'-Fe_4N is assumed to have the atomic structure presented in the text and fully cover the entire surface. For the quadlayer one, an $Fe_2N/Fe_2/Fe_2N/Fe_2$/Cu(001) structure is assumed.

	Fe edge jump		N edge jump	
	Experiment	Calculation	Experiment	Calculation
Monolayer	0.12 (exp.)		0.015 (exp.)	
Bilayer dot	-	0.19	-	0.015
Trilayer	0.32	0.40	0.032	0.034
Quadlayer	-	0.57	-	0.034

Summary

In conclusion, we have investigated electronic and magnetic structures of the γ'-Fe_4N atomic layers on Cu(001). The important findings are summarized in the following.

1. Surface electronic structures of the monolayer γ'-Fe_4N/Cu(001)

Due to the large hybridization between the Fe and N states in the γ'-Fe_4N, the decay of the states at the surface into the vacuum strongly depends on the orbital character. This contrasts with the case of elemental $3d$ systems in which the surface states with particular orbitals dominate the vacuum, and thus no variation is expected for topographic images. The first experimental demonstration of the orbital-selective tunneling process in STM also links the two different images previously reported for the surface with the same symmetry [38, 45].

2. Ferromagnetism of the monolayer γ'-Fe_4N/Cu(001)

The values of the spin magnetic moment estimated from the XMCD measurements show large dependence on the degree of surface lattice ordering, which cannot be distinguished by macroscopic structural characterizations. Due to the Fe-N hybridization and strong two dimensionality of the system, the electronic states of the monolayer γ'-Fe_4N/Cu(001) could take on itinerancy. This renders the ferromagnetism of the system sensitive to the structure even in an atomic scale, which possibly explains the small magnetic moment previously reported within the macroscopic observations [45].

3. Thickness dependence of the electronic/magnetic properties

With the increase of the average sample thickness from monolayer to trilayer, the change in the surface electronic structures as well as the enhancement in the values of the spin magnetic moment has been observed. This clearly originates from the difference in the subsurface layers, especially the stabilization of the subsurface Fe layer in the trilayer γ'-Fe_4N. The layer-resolved DOS calculated by the first principles perfectly explains the experimental results, in terms of the interface sensitive magnetic moments of the Fe atoms.

Overall, the atomically-resolved observation on the sample atomic structure turns out to be indispensable for investigating the physical properties intrinsic to the γ'-Fe_4N atomic layers. The present study demonstrates a close interplay between the microscopic atomic structure and the electronic/magnetic properties of the system, by combining the complementary multiple methods.

The new observations here can also be a guide to the future experiments. The variation in the STM topographic images depending on the tip-surface distance was considered negligible so far. However, the present results establish the importance of the tip-surface distance as a measurement parameter, to be taken into account especially in the STM measurements on multielement/complex surfaces. Utilizing the orbital-dependent decay length could then pave the new way to experimentally identify the orbital character of the states decaying into the vacuum by detailed STM/STS experiments. It is also revealed that, for the systems with itinerant electronic states, the defect in an atomic level largely affects the surrounding electronic structures. The impact of the atomic-scale disorder on the thin-film ferromagnetism was previously underestimated, but the characterization from both microscopic and macroscopic points of views would be necessary for the quantitative discussion on ferromagnetism particularly in an atomic-layer limit.

Finally, we briefly mention future prospects. The γ'-Fe_4N/Cu(001) is a unique monolayer $3d$ ferromagnet on a metallic substrate and has a robust structure toward external perturbations such as the tip-induced force, oxidization, or contamination. That means, the present system will be a good template to investigate an intrinsic interaction between an adsorbate and ferromagnetic substrate; in particular, comparing the results with those on a common monolayer insulator of Cu_2N/Cu(001) with similar $c(2 \times 2)$ symmetry [126, 127], the role of a ferromagnetic interaction on physical properties including magnetic anisotropy, life time of magnetization, or Kondo effect could be understood. Furthermore, spin-polarized STM measurements [128] would give the additional information on the electronic and magnetic structures of the γ'-Fe_4N/Cu(001): the orbital-selective tunneling process possibly shows clear difference with respect to the spin channel, and the spin polarization around the atomic defect could inform the in-plane spin-dependent decay length of the ferromagnetic interaction.

Acknowledgements

First of all, it is my pleasure to express sincere gratitude to my supervisor Prof. Fumio Komori, guiding me to a fruitful research field of surface science. Your sound advice and profound knowledge on physics always help my research life. Then, I would like to express my great thanks to Dr. Toshio Miyamachi, my first and best teacher of STM. I have learned a lot from your attitude toward experiments as well, often motivated and guided me to the better direction.

I would thank the members of Komori group: Mr. Norikazu Kawamura, Mr. Takushi Iimori, Dr. Masamichi Yamada, Mr. Shuhei Nakashima and Mr. Takuma Hattori for warm supports during my Ph.D life. Also I would appreciate the cooperation of the former members, Dr. Koichiro Ienaga, Dr. Sunghun Kim, Mr. Sogen Toyohisa, and Mr. Tadashi Tamura. I could spend wonderful time in the laboratory with all of you.

The basics of magnetism and synchrotron-based measurements have been developed during my master course. To the members of Fujimori group, especially Prof. Atsushi Fujimori and Mr. Goro Shibata, I would be grateful for teaching me a lot of things being my base of scientific research.

I would appreciate courtesy of Dr. Toshihiko Yokoyama, Dr. Yasumasa Takagi, and Ms. Madoka Uozumi during the beamtime in UVSOR. I would also like to thank Dr. Arthur Ernst and Dr. Victor Antonov for strong theoretical supports.

The three-month stay in Barcelona has changed me a lot, given a number of beautiful experience and confidence being as a global scientist. I would be most grateful to Prof. Aitor Mugarza for organizing and supporting everything, and all the members in Mugarza group as well. For Ms. Natsumi Ishibashi and Ms. Michiko Komaki, I would appreciate dealing with a number of works and giving me encouragement.

Finally, I would like to thank my parents and relatives for supporting my student life as well as research activities.

February 2017
Yukio Takahashi

References

[1] N. F. Mott, Proc. Phys. Soc. London **47**, 571 (1935).

[2] D. G. Pettifor, J. Phys. C **3**, 367 (1970).

[3] J. Goodenough, *Magnetism and Crystal Structure in Nonmetals*, *Technical report (Lincoln Laboratory)* (Defense Technical Information Center, 1962).

[4] N. F. Mott, Proc. Phys. Soc. London, Sect. A **62**, 416 (1949).

[5] O. Gunnarsson, J. Phys. F **6**, 587 (1976).

[6] V. L. Moruzzi, P. M. Marcus, K. Schwarz, and P. Mohn, Phys. Rev. B **34**, 1784 (1986).

[7] J. Coey, *Magnetism and Magnetic Materials* (Cambridge University Press, 2010).

[8] M. N. Baibich, J. M. Broto, A. Fert, F. N. Van Dau, F. Petroff, P. Etienne, G. Creuzet, A. Friederich, and J. Chazelas, Phys. Rev. Lett. **61**, 2472 (1988).

[9] R. von Helmolt, J. Wecker, B. Holzapfel, L. Schultz, and K. Samwer, Phys. Rev. Lett. **71**, 2331 (1993).

[10] J. Mathon and A. Umerski, Phys. Rev. B **63**, 220403 (2001).

[11] S. Yuasa, A. Fukushima, H. Kubota, Y. Suzuki, and K. Ando, Appl. Phys. Lett. **89**, 042505 (2006).

[12] M. Uehara, S. Mori, C. H. Chen, and S. W. Cheong, Nature **399**, 560 (1999).

[13] A. P. Ramirez, J. Phys.: Condens. Matter **9**, 8171 (1997).

[14] M. Sagawa, S. Fujimura, N. Togawa, H. Yamamoto, and Y. Matsuura, J. Appl. Phys. **55**, 2083 (1984).

[15] O. A. Ovanov, L. V. Solina, and V. A. Demshina, Phys. Met. Metallogr. **35**, 81 (1973).

[16] T. Burkert, L. Nordström, O. Eriksson, and O. Heinonen, Phys. Rev. Lett. **93**, 027203 (2004).

[17] T. Shima, M. Okamura, S. Mitani, and K. Takanashi, J. Magn. Magn. Mater. **310**, 2213 (2007).

[18] L. Toth, *Transition metal carbides and nitrides*, *Refractory materials* (Academic Press, 1971).

[19] C.-M. Fang, R. S. Koster, W.-F. Li, and M. A. van Huis, RSC Adv. **4**, 7885 (2014).

[20] K. M. Ching, W. D. Chang, T. S. Chin, J. G. Duh, and H. C. Ku, J. Appl. Phys. **76**, 6582 (1994).

[21] S. Dhar, O. Brandt, and K. H. Ploog, Appl. Phys. Lett. **86**, (2005).

[22] Y. Yasutomi, K. Ito, T. Sanai, K. Toko, and T. Suemasu, J. Appl. Phys. **115**, 17A935 (2014).

[23] K. Ito, K. Harada, K. Toko, M. Ye, A. Kimura, Y. Takeda, Y. Saitoh, H. Akinaga, and T. Suemasu, Appl. Phys. Lett. **99**, (2011).

[24] Y. Takahashi, Y. Imai, and T. Kumagai, J. Magn. Magn. Mater. **323**, 2941 (2011).

[25] Y. Komasaki, M. Tsunoda, S. Isogami, and M. Takahashi, J. Appl. Phys. **105**, 07C928 (2009).

[26] K. Sunaga, M. Tsunoda, K. Komagaki, Y. Uehara, and M. Takahashi, J. Appl. Phys. **102**, (2007).

[27] K. Ito, G. H. Lee, H. Akinaga, and T. Suemasu, J. Cryst. Growth **322**, 63 (2011).

[28] K. Ito, K. Harada, K. Toko, H. Akinaga, and T. Suemasu, J. Cryst. Growth **336**, 40 (2011).

[29] P. Srivastava, N. Haack, H. Wende, R. Chauvistré, and K. Baberschke, Phys. Rev. B **56**, R4398 (1997).

[30] M. Farle, W. Platow, A. N. Anisimov, P. Poulopoulos, and K. Baberschke, Phys. Rev. B **56**, 5100 (1997).

[31] M. Farle, B. Mirwald-Schulz, A. N. Anisimov, W. Platow, and K. Baberschke, Phys. Rev. B **55**, 3708 (1997).

[32] B. Schulz and K. Baberschke, Phys. Rev. B **50**, 13467 (1994).

[33] D. Li, M. Freitag, J. Pearson, Z. Q. Qiu, and S. D. Bader, Phys. Rev. Lett. **72**, 3112 (1994).

[34] M. Straub, R. Vollmer, and J. Kirschner, Phys. Rev. Lett. **77**, 743 (1996).

[35] W. Weber, A. Bischof, R. Allenspach, C. H. Back, J. Fassbender, U. May, B. Schirmer, R. M. Jungblut, G. Güntherodt, and B. Hillebrands, Phys. Rev. B **54**, 4075 (1996).

[36] H. L. Meyerheim, J.-M. Tonnerre, L. Sandratskii, H. C. N. Tolentino, M. Przybylski, Y. Gabi, F. Yildiz, X. L. Fu, E. Bontempi, S. Grenier, and J. Kirschner, Phys. Rev. Lett. **103**, 267202 (2009).

[37] B. C. Frazer, Phys. Rev. **112**, 751 (1958).

[38] J. M. Gallego, D. O. Boerma, R. Miranda, and F. Ynduráin, Phys. Rev. Lett. **95**, 136102 (2005).

[39] J. M. Gallego, S. Y. Grachev, M. C. G. Passeggi, F. Sacharowitz, D. Ecija, R. Miranda, and D. O. Boerma, Phys. Rev. B **69**, 121404 (2004).

[40] C. Navio, J. Alvarez, M. J. Capitan, D. Ecija, J. M. Gallego, F. Yndurain, and R. Miranda, Phys. Rev. B **75**, 125422 (2007).

[41] A. Sakuma, J. Phys. Soc. Jpn. **60**, 2007 (1991).

[42] G. Shirane, W. J. Takei, and S. L. Ruby, Phys. Rev. **126**, 49 (1962).

[43] S. Kokado, N. Fujima, K. Harigaya, H. Shimizu, and A. Sakuma, Phys. Rev. B **73**, 172410 (2006).

[44] J. M. Gallego, S. Y. Grachev, D. M. Borsa, D. O. Boerma, D. Écija, and R. Miranda, Phys. Rev. B **70**, 115417 (2004).

[45] Y. Takagi, K. Isami, I. Yamamoto, T. Nakagawa, and T. Yokoyama, Phys. Rev. B **81**, 035422 (2010).

[46] O. N. Mryasov, V. A. Gubanov, and A. I. Liechtenstein, Phys. Rev. B **45**, 12330 (1992).

[47] C. T. Chen, Y. U. Idzerda, H.-J. Lin, N. V. Smith, G. Meigs, E. Chaban, G. H. Ho, E. Pellegrin, and F. Sette, Phys. Rev. Lett. **75**, 152 (1995).

[48] E. H. Sondheimer, Adv. Phys. **50**, 499 (2001).

[49] B. T. Thole, P. Carra, F. Sette, and G. van der Laan, Phys. Rev. Lett. **68**, 1943 (1992).

[50] P. Carra, B. T. Thole, M. Altarelli, and X. Wang, Phys. Rev. Lett. **70**, 694 (1993).

[51] J. Stöhr and H. König, Phys. Rev. Lett. **75**, 3748 (1995).

[52] T. Koide, H. Miyauchi, J. Okamoto, T. Shidara, A. Fujimori, H. Fukutani, K. Amemiya, H. Takeshita, S. Yuasa, T. Katayama, and Y. Suzuki, Phys. Rev. Lett. **87**, 257201 (2001).

[53] R. Shankar, *Principles of Quantum Mechanics (2nd ed.)* (Kluwer Academic/Plenum Publishers, 1994).

[54] R. Wiesendanger, *Scanning Probe Microscopy and Spectroscopy: Methods and Applications* (Cambridge University Press, 1994).

[55] J. Bardeen, Phys. Rev. Lett. **6**, 57 (1961).

[56] J. Tersoff and D. R. Hamann, Phys. Rev. Lett. **50**, 1998 (1983).

[57] J. Tersoff and D. R. Hamann, Phys. Rev. B **31**, 805 (1985).

[58] V. A. Ukraintsev, Phys. Rev. B **53**, 11176 (1996).

[59] T. Gejo, Y. Takata, T. Hatsui, M. Nagasono, H. Oji, N. Kosugi, and E. Shigemasa, Chem. Phys. **289**, 15 (2003).

[60] M. C. Hettrick, J. H. Underwood, P. J. Batson, and M. J. Eckart, Appl. Opt. **27**, 200 (1988).

[61] T. Nakagawa, Y. Takagi, Y. Matsumoto, and T. Yokoyama, Jpn. J. Appl. Phys. **47**, 2132 (2008).

[62] T. Choi, C. D. Ruggiero, and J. A. Gupta, Phys. Rev. B **78**, 035430 (2008).

[63] Y. Nakamura, Y. Kondo, J. Nakamura, and S. Watanabe, Phys. Rev. Lett. **87**, 156102 (2001).

[64] S. Heinze, S. Blügel, R. Pascal, M. Bode, and R. Wiesendanger, Phys. Rev. B **58**, 16432 (1998).

[65] E. J. van Loenen, J. E. Demuth, R. M. Tromp, and R. J. Hamers, Phys. Rev. Lett. **58**, 373 (1987).

[66] G. M. Rutter, N. P. Guisinger, J. N. Crain, E. A. A. Jarvis, M. D. Stiles, T. Li, P. N. First, and J. A. Stroscio, Phys. Rev. B **76**, 235416 (2007).

[67] G. Doyen, D. Drakova, J. V. Barth, R. Schuster, T. Gritsch, R. J. Behm, and G. Ertl, Phys. Rev. B **48**, 1738 (1993).

[68] M. Böhringer, W.-D. Schneider, R. Berndt, K. Glöckler, M. Sokolowski, and E. Umbach, Phys. Rev. B **57**, 4081 (1998).

[69] J. A. Stroscio, D. T. Pierce, A. Davies, R. J. Celotta, and M. Weinert, Phys. Rev. Lett. **75**, 2960 (1995).

[70] F. Calleja, A. Arnau, J. J. Hinarejos, A. L. Vázquez de Parga, W. A. Hofer, P. M. Echenique, and R. Miranda, Phys. Rev. Lett. **92**, 206101 (2004).

[71] A. Picone, G. Fratesi, A. Brambilla, P. Sessi, F. Donati, S. Achilli, L. Maini, M. I. Trioni, C. S. Casari, M. Passoni, A. Li Bassi, M. Finazzi, L. Duò, and F. Ciccacci, Phys. Rev. B **81**, 115450 (2010).

[72] A. Tange, C. L. Gao, B. Y. Yavorsky, I. V. Maznichenko, C. Etz, A. Ernst, W. Hergert, I. Mertig, W. Wulfhekel, and J. Kirschner, Phys. Rev. B **81**, 195410 (2010).

[73] T. Woolcot, G. Teobaldi, C. L. Pang, N. S. Beglitis, A. J. Fisher, W. A. Hofer, and G. Thornton, Phys. Rev. Lett. **109**, 156105 (2012).

[74] S. Driver and D. Woodruff, Surf. Sci. **442**, 1 (1999).

[75] F. Komori, S. Ohno, and K. Nakatsuji, Prog. Surf. Sci. **77**, 1 (2004).

[76] L. Gerhard, T. K. Yamada, T. Balashov, A. F. Takacs, R. J. H. Wesselink, M. Dane, M. Fechner, S. Ostanin, A. Ernst, I. Mertig, and W. Wulfhekel, Nat. Nano. **5**, 792 (2010).

[77] J. G. Simmons, J. Appl. Phys. **34**, 1793 (1963).

[78] B. J. van Wees, H. van Houten, C. W. J. Beenakker, J. G. Williamson, L. P. Kouwenhoven, D. van der Marel, and C. T. Foxon, Phys. Rev. Lett. **60**, 848 (1988).

[79] C. Julian Chen, *Introduction to Scanning Tunneling Microscopy* (Oxford University Press, 1993).

[80] S. F. Alvarado, Phys. Rev. Lett. **75**, 513 (1995).

[81] M. Eltschka, B. Jäck, M. Assig, O. V. Kondrashov, M. A. Skvortsov, M. Etzkorn, C. R. Ast, and K. Kern, Nano Lett. **14**, 7171 (2014).

[82] A. H. Castro Neto, F. Guinea, N. M. R. Peres, K. S. Novoselov, and A. K. Geim, Rev. Mod. Phys. **81**, 109 (2009).

[83] J. R. Schaibley, H. Yu, G. Clark, P. Rivera, J. S. Ross, K. L. Seyler, W. Yao, and X. Xu, Nat. Rev. Mater. **1**, 16055 (2016).

[84] J. Lahiri, Y. Lin, P. Bozkurt, I. I. Oleynik, and M. Batzill, Nat. Nanotechnol. **5**, 326 (2010).

[85] Y.-C. Lin, T. Björkman, H.-P. Komsa, P.-Y. Teng, C.-H. Yeh, F.-S. Huang, K.-H. Lin, J. Jadczak, Y.-S. Huang, P.-W. Chiu, A. V. Krasheninnikov, and K. Suenaga, Nat. Commun. **6**, 6736 (2015).

[86] O. V. Yazyev and L. Helm, Phys. Rev. B **75**, 125408 (2007).

[87] M. M. Ugeda, I. Brihuega, F. Guinea, and J. M. Gómez-Rodríguez, Phys. Rev. Lett. **104**, 096804 (2010).

[88] J. Haskins, A. Knac, C. Sevik, H. Sevinçli, G. Cuniberti, and T. Çağn, ACS Nano **5**, 3779 (2011).

[89] O. V. Yazyev and S. G. Louie, Nat. Mater. **9**, 806 (2010).

[90] Y. Wei, J. Wu, H. Yin, X. Shi, R. Yang, and M. Dresselhaus, Nat. Mater. **11**, 759 (2012).

[91] Q. Yu, L. A. Jauregui, W. Wu, R. Colby, J. Tian, Z. Su, H. Cao, Z. Liu, D. Pandey, D. Wei, T. F. Chung, P. Peng, N. P. Guisinger, E. A. Stach, J. Bao, S.-S. Pei, and Y. P. Chen, Nat. Mater. **10**, 443 (2011).

[92] A. M. van der Zande, P. Y. Huang, D. A. Chenet, T. C. Berkelbach, Y. You, G.-H. Lee, T. F. Heinz, D. R. Reichman, D. A. Muller, and J. C. Hone, Nat. Mater. **12**, 554 (2013).

[93] W. Zhou, X. Zou, S. Najmaei, Z. Liu, Y. Shi, J. Kong, J. Lou, P. M. Ajayan, B. I. Yakobson, and J.-C. Idrobo, Nano Lett. **13**, 2615 (2013).

[94] F. Banhart, J. Kotakoski, and A. V. Krasheninnikov, ACS Nano **5**, 26 (2011).

[95] F. Donati, S. Rusponi, S. Stepanow, C. Wäckerlin, A. Singha, L. Persichetti, R. Baltic, K. Diller, F. Patthey, E. Fernandes, J. Dreiser, Ž. Šljivančanin, K. Kummer, C. Nistor, P. Gambardella, and H. Brune, Science **352**, 318 (2016).

[96] I. G. Rau, S. Baumann, S. Rusponi, F. Donati, S. Stepanow, L. Gragnaniello, J. Dreiser, C. Piamonteze, F. Nolting, S. Gangopadhyay, O. R. Albertini, R. M. Macfarlane, C. P. Lutz, B. A. Jones, P. Gambardella, A. J. Heinrich, and H. Brune, Science **344**, 988 (2014).

[97] Y. Takahashi, T. Miyamachi, K. Ienaga, N. Kawamura, A. Ernst, and F. Komori, Phys. Rev. Lett. **116**, 056802 (2016).

[98] Y. Takahashi, T. Miyamachi, S. Nakashima, N. Kawamura, Y. Takagi, M. Uozumi, V. Antonov, T. Yokoyama, A. Ernst, and F. Komori, arXiv:1702.01509 (2017).

[99] R. Nakajima, J. Stöhr, and Y. U. Idzerda, Phys. Rev. B **59**, 6421 (1999).

[100] G. Ganteför and W. Eberhardt, Phys. Rev. Lett. **76**, 4975 (1996).

[101] J. Coey and P. Smith, J. Magn. Magn. Mater. **200**, 405 (1999).

[102] J. M. D. Coey, J. Appl. Phys. **76**, 6632 (1994).

[103] M. Komuro, Y. Kozono, M. Hanazono, and Y. Sugita, J. Appl. Phys. **67**, 5126 (1990).

[104] C. Ortiz, G. Dumpich, and A. H. Morrish, Applied Physics Letters **65**, 2737 (1994).

[105] S. Atiq, H.-S. Ko, S. A. Siddiqi, and S.-C. Shin, Appl. Phys. Lett. **92**, (2008).

[106] D. M. Borsa, S. Grachev, D. O. Boerma, and J. W. J. Kerssemakers, Appl. Phys. Lett. **79**, 994 (2001).

[107] K. Ito, G. H. Lee, K. Harada, M. Suzuno, T. Suemasu, Y. Takeda, Y. Saitoh, M. Ye, A. Kimura, and H. Akinaga, Appl. Phys. Lett. **98**, (2011).

[108] K. R. Nikolaev, I. N. Krivorotov, E. D. Dahlberg, V. A. Vas'ko, S. Urazhdin, R. Loloee, and W. P. Pratt, Appl. Phys. Lett. **82**, 4534 (2003).

[109] K. Ito, K. Toko, Y. Takeda, Y. Saitoh, T. Oguchi, T. Suemasu, and A. Kimura, J. Appl. Phys. **117**, (2015).

[110] S. H. Kim, K. S. Lee, H. G. Min, J. Seo, S. C. Hong, T. H. Rho, and J.-S. Kim, Phys. Rev. B **55**, 7904 (1997).

[111] F. Nouvertné, U. May, M. Bamming, A. Rampe, U. Korte, G. Güntherodt, R. Pentcheva, and M. Scheffler, Phys. Rev. B **60**, 14382 (1999).

[112] P. Torelli, F. Sirotti, and P. Ballone, Phys. Rev. B **68**, 205413 (2003).

[113] J. P. Perdew and Y. Wang, Phys. Rev. B **45**, 13244 (1992).

[114] M. Lüders, A. Ernst, W. M. Temmerman, Z. Szotek, and P. J. Durham, J. Phys.: Condens. Matter **13**, 8587 (2001).

[115] M. Geilhufe, S. Achilles, M. A. Köbis, M. Arnold, I. Mertig, W. Hergert, and A. Ernst, J. Phys.: Condens. Matter **27**, 435202 (2015).

[116] T. Detzel and N. Memmel, Phys. Rev. B **49**, 5599 (1994).

[117] N. Memmel and T. Detzel, Surf. Sci. **307**, 490 (1994).

[118] J. Shen, J. Giergiel, A. Schmid, and J. Kirschner, Surf. Sci. **328**, 32 (1995).

[119] G. Bayreuther, F. den Broeder, D. Chambliss, K. Johnson, R. Wilson, and S. Chiang, J. Magn. Magn. Mater. **121**, 1 (1993).

[120] Y. B. Xu, E. T. M. Kernohan, D. J. Freeland, A. Ercole, M. Tselepi, and J. A. C. Bland, Phys. Rev. B **58**, 890 (1998).

[121] J. Tersoff and L. M. Falicov, Phys. Rev. B **26**, 6186 (1982).

[122] O. Hjortstam, J. Trygg, J. M. Wills, B. Johansson, and O. Eriksson, Phys. Rev. B **53**, 9204 (1996).

[123] D. Pescia, M. Stampanoni, G. L. Bona, A. Vaterlaus, R. F. Willis, and F. Meier, Phys. Rev. Lett. **58**, 2126 (1987).

[124] R. Lorenz and J. Hafner, Phys. Rev. B **54**, 15937 (1996).

[125] P. Bruno, Phys. Rev. B **39**, 865 (1989).

[126] C. F. Hirjibehedin, C.-Y. Lin, A. F. Otte, M. Ternes, C. P. Lutz, B. A. Jones, and A. J. Heinrich, Science **317**, 1199 (2007).

[127] A. F. Otte, M. Ternes, K. von Bergmann, S. Loth, H. Brune, C. P. Lutz, C. F. Hirjibehedin, and A. J. Heinrich, Nat. Phys. **4**, 847 (2008).

[128] R. Wiesendanger, H.-J. Güntherodt, G. Güntherodt, R. J. Gambino, and R. Ruf, Phys. Rev. Lett. **65**, 247 (1990).